EUROPEAN COMMISSION

Community Research

# MATISSE

Materials' Innovations for Safe and Sustainable nuclear in Europe

**Support to the development of joint research actions between national programmes on advanced nuclear materials**

FP7-Fission-2013
Combination of Collaborative project (CP) and Coordination and Support Actions (CSA)

Grant agreement no: 604862
Start date: 01/11/2013 Duration: 48 Months

---

***D.2.51***

# *Rationalization of irradiation hardening data in Fe-Cr-NiSiP alloys by means of dislocation dynamics or other models*

---

**MatISSE** – Contract Number: 604862

| | |
|---|---|
| Document title | Screening of irradiation creep mechanisms using atomic-level simulation tools |
| Author(s) | Emmanuel Clouet (CEA), Alexander Bakaev (HZDR), Vladimir Borodin (KIT), Z. Chang (KTH), C. C. Fu (CEA), M. C. Marinica (CEA), P. Olsson (KTH), M. Posselt (HZDR), D. Terentyev (SCK•CEN), P. Vladimirov (KIT), E. E. Zhurkin (St Petersburg Univ.) |
| Number of pages | 40 |
| Document type | Deliverable |
| Work Package | 2 |
| Document number | D2.51 |
| Issued by | CEA |
| Date of completion | 17/11/2017 |
| Dissemination level | Confidential, only for consortium members (including the Commission Services) |

**Summary**

We report on the use of atomistic simulations to examine the different mechanisms which are relevant for irradiation creep and which need to be considered for the development of models at an upper scale, like crystal plasticity and cluster dynamics. Ab initio calculations are first used to characterize the coupling of point-defects, both vacancies and self-interstitials, with an applied elastic field. The comparison of these results with those obtained with empirical potentials allows the validity of the latter to be assessed, when describing the coupling of point-defect diffusion with an applied stress. An empirical potential is then used to calculate the dependence of the dislocation bias factor, i.e. the imbalance between vacancy and self-interstitials absorption by the dislocation, and its variation with the applied stress. Finally, molecular dynamics simulations are performed to study the possible influence of slip band interaction with nanostructural defects on irradiation creep.

**Approval**

| Rev. | Date | First author | WP leader | Project Coordinator |
|---|---|---|---|---|
| 0 | 11/2017 | E. Clouet (CEA) | L. Malerba (SCK•CEN) | P.F. Giroux (CEA) |
| | | 20/10/2017 | 29/10/2017 | 17/11/2017 |


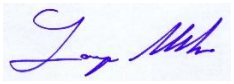


**Distribution list**

| Name | Organisation | Comments |
|---|---|---|
| All beneficiaries | MatISSE | |

**Table of contents**

# 1. Point-defect interaction with a stress field

This section describes the work performed at CEA SRMP. Its purpose is to use ab initio calculations to characterize the coupling of point-defects, both vacancy and self-interstitial atom (SIA) with an applied stress and to validate the empirical potentials used to calculate, by atomistic simulations, the dislocation biases (see next section). We use, for this purpose, the elastic description of a point-defect and extract the input parameters from atomistic simulations, relying either on ab-initio calculations or on empirical potentials. This enables the characterization of point-defect coupling with an applied stress to be done using a reduced number of parameters and thus to easily compare the different energy models.

## 1 Elastic model of a point-defect

### 1. Elastic dipole

Different models can be used to describe a point-defect within elasticity theory. One such model is the elastic dipole description. We first introduce this model and show how the parameters can be obtained with atomistic simulations.

A point-defect can be described in a continuous solid body as an equilibrated distribution of point forces [1-4], i.e. a distribution with neither net force nor torque. Keeping only the first moment of this distribution, the defect is fully characterized by its elastic dipole $\boldsymbol{P_{ij}}$. This elastic dipole is a symmetric second-rank tensor having the symmetry of the point-defect.

The interaction energy of the point defect with an external elastic field, either the elastic field arising from another defect or an applied elastic field, is then simply given by

$$\boldsymbol{E}^{\text{int}} = -\boldsymbol{P_{ij}}\varepsilon_{\boldsymbol{ij}}^{\text{ext}}(\vec{0}), \tag{1.1}$$

where $\varepsilon_{\boldsymbol{ij}}^{\text{ext}}(\vec{0})$ is the strain of the external elastic field at the location of the point-defect. In this equation and in the following we use Einstein summation convention: summations over Cartesian repeated indices are implicit. Higher order contributions to the interaction energy involve successive gradient of the external strain field coupling with higher moments of the multipole expansion of the force distribution and can be generally safely ignored. This simple expression of the interaction energy is the workhorse of the modelling of point-defects within linear elasticity in a multiscale approach.

The Eshelby inclusion [5,6] is another widespread model which can be used to describe a point-defect in an elastic continuum. One can show that the elastic dipole is equivalent to the Eshelby inclusion in the limit of an infinitesimal inclusion. The same analogy holds with an infinitesimal dislocation loop.

### 2. Polarizability

In some irradiation creep models it is not enough to describe the point-defect solely by its elastic dipole. One also needs to consider that the properties of a point-defect can be altered by an applied elastic field [7]. This applied elastic field thus leads to an induced elastic dipole, so the total elastic dipole of the point-defect now depends on the applied strain $\varepsilon_{\boldsymbol{ij}}^{\text{ext}}(\vec{0})$:

$$\boldsymbol{P_{ij}}(\varepsilon^{\text{ext}}) = \boldsymbol{P_{ij}^0} + \alpha_{\boldsymbol{ijkl}}\varepsilon_{\boldsymbol{kl}}^{\text{ext}}, \tag{1.2}$$

where $\boldsymbol{P_{ij}^0}$ is the permanent elastic dipole in absence of applied strain and $\alpha_{\boldsymbol{ijkl}}$ is the point-defect dia-elastic polarizability [8,9], a fourth-rank tensor having the symmetry of the point-defect. Considering the analogy with Eshelby's inclusion, this polarizability corresponds to an infinitesimal inhomogeneous inclusion, i.e. an inclusion with different elastic constants than the surrounding matrix. It describes the fact that the matrix close to the point defect have a different elastic response to an applied strain because of the perturbations of the atomic bonding caused by the point-defect. For the analogy with an infinitesimal dislocation loop, the polarizability corresponds to the fact that

the loop can change its shape by glide on its prismatic cylinder (or in its habit plane for a pure glide loop) under the action of the applied elastic field.

Following Schober [8], the interaction of a point-defect located at the origin with an applied strain is now given by

$$\boldsymbol{E}^{\text{int}} = -\boldsymbol{P}_{ij}^{0}\varepsilon_{ij}^{\text{ext}}(\vec{0}) - \frac{1}{2}\alpha_{ijkl}\varepsilon_{ij}^{\text{ext}}(\vec{0})\varepsilon_{kl}^{\text{ext}}(\vec{0}). \tag{1.3}$$

This expression of the interaction energy, considering the polarizability, has important consequences for the modeling of point-defects, as it shows that some coupling is possible between two different applied elastic fields. Considering the point defect interaction with two strain fields $\varepsilon^{(1)}$ and $\varepsilon^{(2)}$ originating from two different sources, the interaction energy is now given by

$$\begin{aligned}\boldsymbol{E}^{\text{int}} &= -\boldsymbol{P}_{ij}^{0}\left(\varepsilon_{ij}^{(1)}+\varepsilon_{ij}^{(2)}\right) - \frac{1}{2}\alpha_{ijkl}\left(\varepsilon_{ij}^{(1)}+\varepsilon_{ij}^{(2)}\right)\left(\varepsilon_{kl}^{(1)}+\varepsilon_{kl}^{(2)}\right) \\ &= -\boldsymbol{P}_{ij}^{0}\varepsilon_{ij}^{(1)} - \frac{1}{2}\alpha_{ijkl}\varepsilon_{ij}^{(1)}\varepsilon_{kl}^{(1)} - \boldsymbol{P}_{ij}^{0}\varepsilon_{ij}^{(2)} - \frac{1}{2}\alpha_{ijkl}\varepsilon_{ij}^{(2)}\varepsilon_{kl}^{(2)} - \alpha_{ijkl}\varepsilon_{ij}^{(1)}\varepsilon_{kl}^{(2)}\end{aligned}. \tag{1.4}$$

The last term in the second line shows that, without the polarizability, the interaction energy of the point defects with the two strain fields will be simply the superposition of the two interaction energies with each strain fields considered separately. A coupling is introduced only through the polarizability. Such a coupling is for instance at the origin of one of the mechanisms proposed to explain creep under irradiation. Because of the polarizability, the interaction of point-defects, either vacancies or self-interstitial atoms, with dislocations under an applied stress depends on the dislocation orientation with respect to the applied stress. This stronger interaction with some dislocation families leads to a larger drift term in the diffusion equation of the point-defect and thus to a greater absorption of the point-defect by these dislocations, a mechanism known as Stress Induced Preferential Absorption (or SIPA) [10]. This polarizability is also the cause, in alloy solid solutions, of the variation of the matrix elastic constants with their solute content.

This dia-elastic polarizability caused by the perturbation of the elastic response of the surrounding matrix manifests itself at the lowest temperature, even 0 K, and whatever the characteristic time of the applied strain. At finite temperature there may be another source of polarizability. If the point-defect can adopt different configurations, for instance different variants corresponding to different orientations of the point-defect like for a carbon interstitial atom in a body-centered cubic Fe matrix, then the occupancy distribution of these configurations will be modified under an applied stress. For an oscillatory applied strain, this possible redistribution of the point defect gives rise to anelasticity [11], the most famous case being the Snoek relaxation in iron alloys containing interstitial solute atoms like C and N [12]. When thermally activated transitions between the different configurations of the point-defect are fast enough compared to the characteristic time of the applied stress, the distribution of the different configurations corresponds to thermal equilibrium. Assuming that all configurations have the same energy in a stress-free state $\mu$ and denoting by $\boldsymbol{P}_{ij}^{\mu}$ the elastic dipole of the configuration μ, the average dipole of the point-defect is then given by

$$\langle \boldsymbol{P}_{ij} \rangle = \frac{\sum_{\mu} \exp\left(-\boldsymbol{P}_{kl}^{\mu}\varepsilon_{kl}^{\text{ext}}/\boldsymbol{kT}\right)\boldsymbol{P}_{ij}^{\mu}}{\sum_{\mu} \exp\left(-\boldsymbol{P}_{kl}^{\mu}\varepsilon_{kl}^{\text{ext}}/\boldsymbol{kT}\right)} \tag{1.5}$$

As a consequence, the average elastic dipole of the point-defect distribution is now depending on applied stress and temperature, an effect known as para-elasticity [7]. At temperatures high enough to allow the transition between the different configurations, the interaction energy of the configurations with the applied strain is usually small compared to $\boldsymbol{kT}$. One can make a limited expansion of the exponentials to obtain

$$\langle \boldsymbol{P}_{ij} \rangle = \sum_{\mu} \boldsymbol{P}_{ij}^{\mu} - \sum_{\mu} \frac{\boldsymbol{P}_{ij}^{\mu}\boldsymbol{P}_{kl}^{\mu}}{\boldsymbol{kT}}\varepsilon_{kl}^{\text{ext}}. \tag{1.6}$$

This leads to the same linear variation of the elastic dipole with the applied strain as for the dia-elastic polarizability, except that the para-elastic polarizability is depending on the temperature.

In bcc iron, there is no para-elastic polarizability for the vacancy, as it possesses the same symmetries as the host lattice. The vacancy has only a dia-elastic polarizability. On the other hand, the ground state of the SIA is a <110> dumbbell. As this point-defect reduces the symmetry of the bcc lattice, it possesses both a dia- and a para-elastic polarizability.

## 3. Extraction from atomistic simulations

The elastic dipole and the dia-elastic polarizability can be easily extracted from atomistic simulations. Let us consider a simulation box of volume $V$, the equilibrium volume of the bulk material, with periodic boundary conditions, containing one point defect. According to linear elasticity, the variation of the simulation box energy with a homogeneous applied strain is given by

$$\Delta E(\varepsilon_{ij}) = \frac{1}{2} V C_{ijkl} \varepsilon_{ij} \varepsilon_{kl} - P^0_{ij} \varepsilon_{ij} - \frac{1}{2} \alpha_{ijkl} \varepsilon_{ij} \varepsilon_{kl}, \tag{1.7}$$

where $C_{ijkl}$ are the elastic constants of the pristine crystal. One can deduct from this expression the stress tensor:

$$\begin{aligned} \sigma_{ij}(\varepsilon_{ij}) &= \frac{1}{V} \frac{\partial \Delta E}{\partial \varepsilon_{ij}} \\ &= C_{ijkl} \varepsilon_{kl} - \frac{1}{V} \left( P^0_{ij} + \alpha_{ijkl} \varepsilon_{kl} \right) \end{aligned} . \tag{1.8}$$

If the periodicity vectors are fixed to the values of the perfect crystal, i.e. $\varepsilon_{ij} = 0$, the stress is directly proportional to the elastic dipole weighted by the point-defect volume fraction. This residual stress corresponds to the stress increase, after atomic relaxation, due to the introduction of the point-defect into the simulation box. By performing atomic simulations for different applied strains and looking at the variations of the stress (an output of any atomistic code), Eq. 1.8 also allows the point-defect dia-elastic polarizability to be determined. We have used this method to obtain the elastic dipole and the polarizability of the vacancy and of the SIA in bcc iron.

Atomistic simulations are performed calculating the total energy both using ab initio electronic structure calculations and empirical potentials. For the ab initio calculations, we use a supercell of 128 atoms, corresponding to the cubic cell duplicated 4 times in each direction. Calculations are performed with the VASP code [13], using the generalized gradient approximation (GGA) [14]. The interaction between the core and outer electrons is modeled through the projector augmented-wave approximation, considering 3d and 4s electrons in the outer shell. The plane-wave cutoff energy is set at 460 eV and the precision is set to 'accurate'. Relaxation of atomic positions is stopped when all force components are smaller than 10 meV/Å.

For atomistic simulations with empirical potentials, we use various Fe potentials, all of the EAM type: Marinica 07 (potential named M07 in [15,16]), Mendelev 03 [17], Ackland 04 [18], Dudarev 05 [19] and Chiesa 09 [20]. These calculations are performed in a supercell containing 2000 atoms (10x10x10 cubic cell).

## 2 Vacancy in bcc iron

The vacancy does not change the symmetry of the bcc lattice. Its elastic dipole is therefore isotropic (1 component) and its polarizability anisotropic (3 components):

$$\mathbf{P} = \begin{pmatrix} P_{11} & 0 & 0 \\ 0 & P_{11} & 0 \\ 0 & 0 & P_{11} \end{pmatrix} \quad \text{and} \quad \boldsymbol{\alpha} = \begin{pmatrix} \alpha_{1111} & \alpha_{1122} & \alpha_{1122} & 0 & 0 & 0 \\ \alpha_{1122} & \alpha_{1111} & \alpha_{1122} & 0 & 0 & 0 \\ \alpha_{1122} & \alpha_{1122} & \alpha_{1111} & 0 & 0 & 0 \\ 0 & 0 & 0 & \alpha_{1212} & 0 & 0 \\ 0 & 0 & 0 & 0 & \alpha_{1212} & 0 \\ 0 & 0 & 0 & 0 & 0 & \alpha_{1212} \end{pmatrix}.$$

To determine all components of these tensors, we impose three different strains:

- Hydrostatic strain: $\boldsymbol{\varepsilon} = \varepsilon \begin{pmatrix} 1 & 0 & 0 \\ 0 & 1 & 0 \\ 0 & 0 & 1 \end{pmatrix}$

Elasticity theory predicts that the variation of the, when the vacancy is introduced in the simulation box of volume $V$, is given by:

$$\Delta P(\varepsilon) = \frac{1}{V}\left[P_{11} + (\alpha_{1111} + 2\alpha_{1122})\varepsilon\right].$$

The interaction energy of the vacancy with the applied strain should be

$$E^{\text{inter}}(\varepsilon) = -3P_{11}\varepsilon - \frac{3}{2}(\alpha_{1111} + 2\alpha_{1122})\varepsilon^2 .$$

Fitting of the pressure variation given by atomistic simulations allows the single component of the elastic dipole and a combination of two polarizability components to be obtained. We check then that the variations of the energy given by atomistic simulations agree with predictions of elasticity theory using these parameters deduced from the pressure.

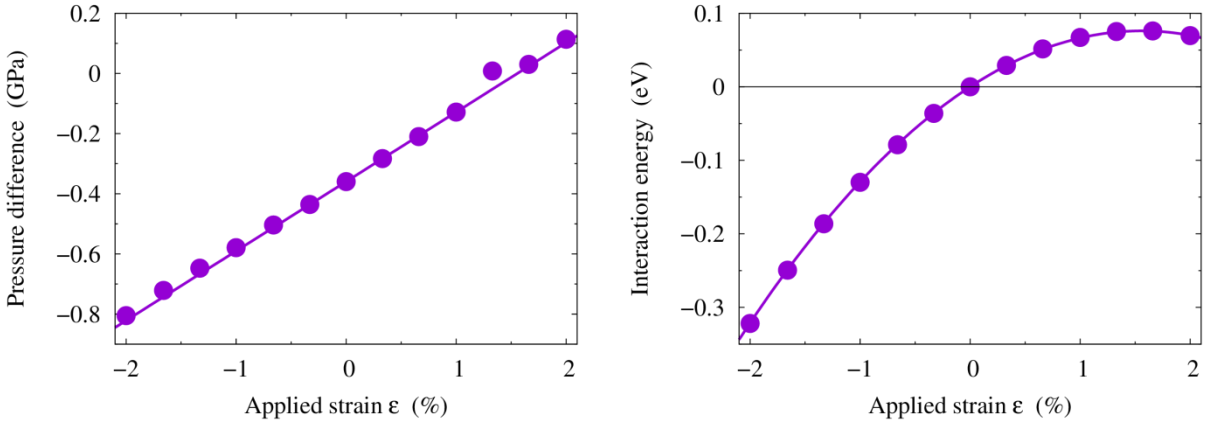


Figure 1: Variation with the hydrostatic strain of the pressure (left) and corresponding interaction energy (right) for the vacancy. Symbols are results of ab initio calculations and solid lines of elastic modelling.

- Shear strain $\boldsymbol{\varepsilon} = \varepsilon \begin{pmatrix} 0 & 1 & 0 \\ 1 & 0 & 0 \\ 0 & 0 & 0 \end{pmatrix}$

The variations of the non-zero components of the stress tensor are then

$$\Delta\sigma_{11}(\varepsilon) = \Delta\sigma_{22}(\varepsilon) = \Delta\sigma_{33}(\varepsilon) = -P_{11}/V ,$$

$$\Delta\sigma_{12}(\varepsilon) = -2\alpha_{1212}\varepsilon/V ,$$

and the interaction energy

$$E^{\text{inter}}(\varepsilon) = -2\,\alpha_{1212}\varepsilon^2 .$$

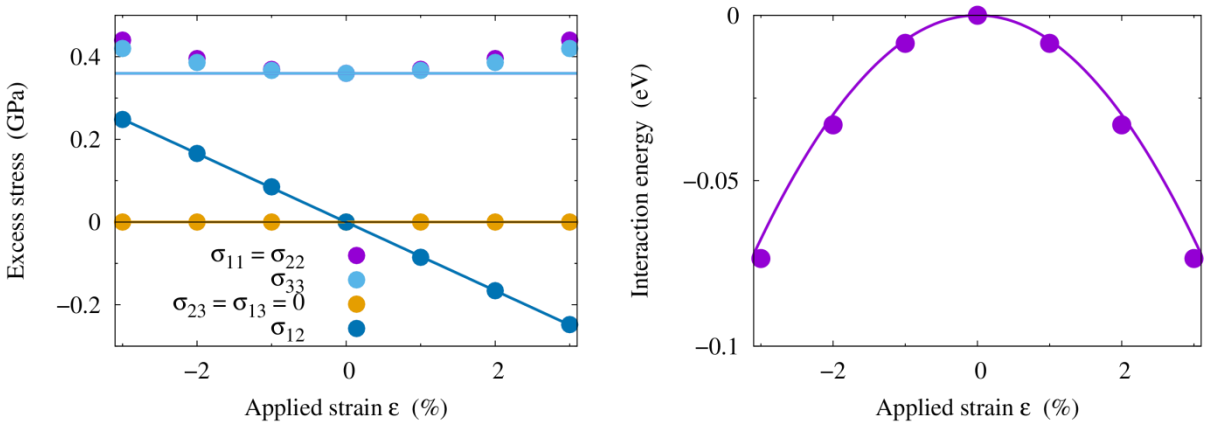


Figure 2: Variation with the shear strain of the stress (left) and corresponding interaction energy (right) for the vacancy. Symbols are results of ab initio calculations and solid lines of elastic modelling.

- Tetragonal strain: $\boldsymbol{\varepsilon} = \varepsilon \begin{pmatrix} -1 & 0 & 0 \\ 0 & -1 & 0 \\ 0 & 0 & 2 \end{pmatrix}$

The variations of the non-zero components of the stress tensor are then

$$\Delta\sigma_{11}(\varepsilon) = \Delta\sigma_{22}(\varepsilon) = -\left[P_{11} + (\alpha_{1122} - \alpha_{1111})\varepsilon\right]/V,$$

$$\Delta\sigma_{33}(\varepsilon) = -\left[P_{11} + 2(\alpha_{1111} - \alpha_{1122})\varepsilon\right]/V,$$

and the interaction energy

$$E^{\text{inter}}(\varepsilon) = -3(\alpha_{1111} - \alpha_{1122})\varepsilon^2.$$

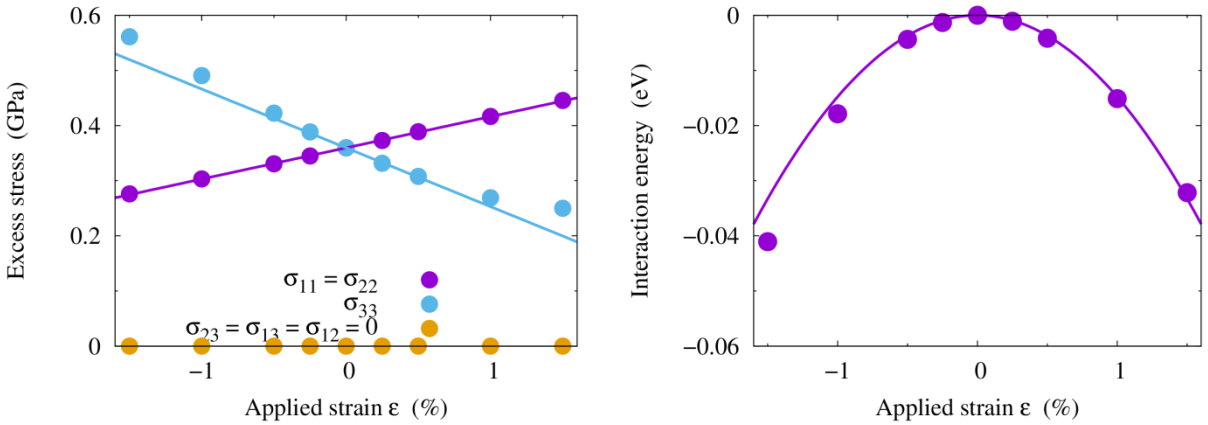


Figure 3: Variation with the tetragonal strain of the stress (left) and corresponding interaction energy (right) for the vacancy. Symbols are results of ab initio calculations and solid lines of elastic modelling.

The components of the elastic dipole and of the polarizability obtained for the vacancy with this approach are given in the table 1 below for ab initio calculations and empirical potentials. All empirical potentials have a reasonable agreement with ab initio calculations.

| | | VASP | Marinica 07 | Mendelev 03 | Ackland 04 | Dudarev 05 | Chiesa 09 |
|---|---|---|---|---|---|---|---|
| Form. energy | $E^f$ (eV) | 2.21 | 2.10 | 1.71 | 1.72 | 1.97 | 1.95 |
| Elastic dipole | $P_{11}$ (eV) | -3.26 | -1.21 | -2.95 | -2.81 | -2.19 | -1.75 |
| Relax. volume | $\Delta V$ ($\Omega$) | -0.23 | -0.094 | -0.23 | -0.24 | -0.17 | -0.14 |
| Polarizability | $\alpha_{1111}$ (eV) | 103 | 63 | 53 | 59 | 50 | 41 |
| | $\alpha_{1122}$ (eV) | 53 | 46 | 40 | 44 | 51 | 32 |
| | $\alpha_{1212}$ (eV) | 38 | 34 | 29 | 31 | 35 | 35 |
| | $\alpha_{1111} + 2\,\alpha_{1122}$ (eV) | 209 | 155 | 133 | 147 | 152 | 105 |

Table 1: Vacancy properties obtained from ab initio calculations (VASP) and various empirical potentials: formation energy, elastic dipole, relaxation volume and polarizability.

## 3 Self-interstitial atom in bcc iron

The ground state of self-interstitial atom (SIA) in bcc iron is the <110> dumbbell. This point-defect lowers the cubic symmetry of the bcc lattice to the orthorhombic symmetry. Its elastic dipole has thus 3 independent components and its polarizability 9 independent components. For the [110] variant of the SIA, these tensors expressed in the cubic axis are given by:

$$\mathbf{P} = \begin{pmatrix} P_{11} & P_{12} & 0 \\ P_{12} & P_{11} & 0 \\ 0 & 0 & P_{33} \end{pmatrix} \quad \text{and} \quad \boldsymbol{\alpha} = \begin{pmatrix} \alpha_{1111} & \alpha_{1122} & \alpha_{1133} & 0 & 0 & \alpha_{1112} \\ \alpha_{1122} & \alpha_{1111} & \alpha_{1133} & 0 & 0 & \alpha_{1112} \\ \alpha_{1133} & \alpha_{1133} & \alpha_{3333} & 0 & 0 & \alpha_{3312} \\ 0 & 0 & 0 & \alpha_{1313} & \alpha_{1323} & 0 \\ 0 & 0 & 0 & \alpha_{1323} & \alpha_{1313} & 0 \\ \alpha_{1112} & \alpha_{1112} & \alpha_{3312} & 0 & 0 & \alpha_{1212} \end{pmatrix}.$$

To determine all components of these tensors, we impose five different strains:

- Hydrostatic strain: $\boldsymbol{\varepsilon} = \varepsilon \begin{pmatrix} 1 & 0 & 0 \\ 0 & 1 & 0 \\ 0 & 0 & 1 \end{pmatrix}$

The variations of the non null components of the stress tensor are then

$$\Delta\sigma_{11}(\varepsilon) = \Delta\sigma_{22}(\varepsilon) = -\left[P_{11} + (\alpha_{1111} + \alpha_{1122} + \alpha_{1133})\varepsilon\right]/V$$
$$\Delta\sigma_{33}(\varepsilon) = -\left[P_{33} + (\alpha_{3333} + 2\alpha_{1133})\varepsilon\right]/V$$
$$\Delta\sigma_{12}(\varepsilon) = -\left[P_{12} + (2\alpha_{1112} + \alpha_{3312})\varepsilon\right]/V$$

and the interaction energy

$$E^{\text{inter}}(\varepsilon) = -(2P_{11} + P_{33})\varepsilon - \frac{1}{2}(2\alpha_{1111} + \alpha_{3333} + 2\alpha_{1122} + 4\alpha_{1133})\varepsilon^2.$$

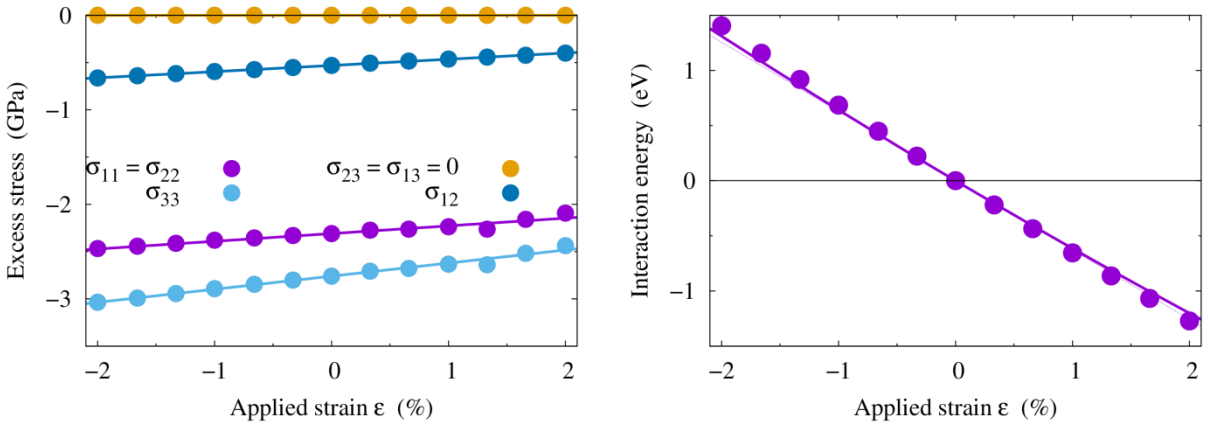


Figure 4: Variation with the hydrostatic strain of the stress (left) and corresponding interaction energy (right) for the vacancy. Symbols are results of ab initio calculations and solid lines of elastic modelling.

- Shear strain in the (100) plane: $\boldsymbol{\varepsilon} = \varepsilon \begin{pmatrix} 0 & 0 & 1 \\ 0 & 0 & 0 \\ 1 & 0 & 0 \end{pmatrix}$

The variations of the non-zero components of the stress tensor are then

$$\Delta\sigma_{11}(\varepsilon) = \Delta\sigma_{22}(\varepsilon) = -P_{11}/V$$
$$\Delta\sigma_{33}(\varepsilon) = -P_{33}/V$$
$$\Delta\sigma_{23}(\varepsilon) = -2\alpha_{2313}\varepsilon/V$$
$$\Delta\sigma_{13}(\varepsilon) = -2\alpha_{1313}\varepsilon/V$$
$$\Delta\sigma_{12}(\varepsilon) = -P_{12}/V$$

and the interaction energy

$$E^{\text{inter}}(\varepsilon) = -2\,\alpha_{1313}\varepsilon^2 .$$

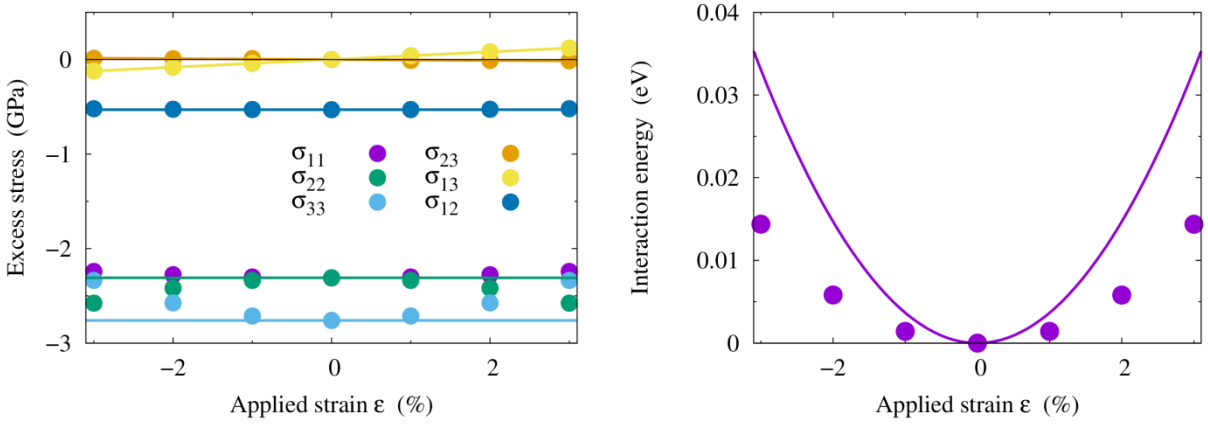


Figure 5: Variation with the shear strain in the (100) plane of the stress (left) and corresponding interaction energy (right) for the vacancy. Symbols are results of ab initio calculations and solid lines of elastic modelling.

- Shear strain in the (001) plane: $\boldsymbol{\varepsilon} = \varepsilon \begin{pmatrix} 0 & 1 & 0 \\ 1 & 0 & 0 \\ 0 & 0 & 0 \end{pmatrix}$

The variations of the non-zero components of the stress tensor are then

$$\Delta\sigma_{11}(\varepsilon) = \Delta\sigma_{22}(\varepsilon) = -\left[P_{11} + 2\alpha_{1112}\varepsilon\right]/V$$
$$\Delta\sigma_{33}(\varepsilon) = -\left[P_{33} + 2\alpha_{3312}\varepsilon\right]/V$$
$$\Delta\sigma_{12}(\varepsilon) = -\left[P_{12} + 2\alpha_{1212}\varepsilon\right]/V$$

and the interaction energy

$$E^{\text{inter}}(\varepsilon) = -2P_{12}\varepsilon - 2\,\alpha_{1212}\varepsilon^2 .$$

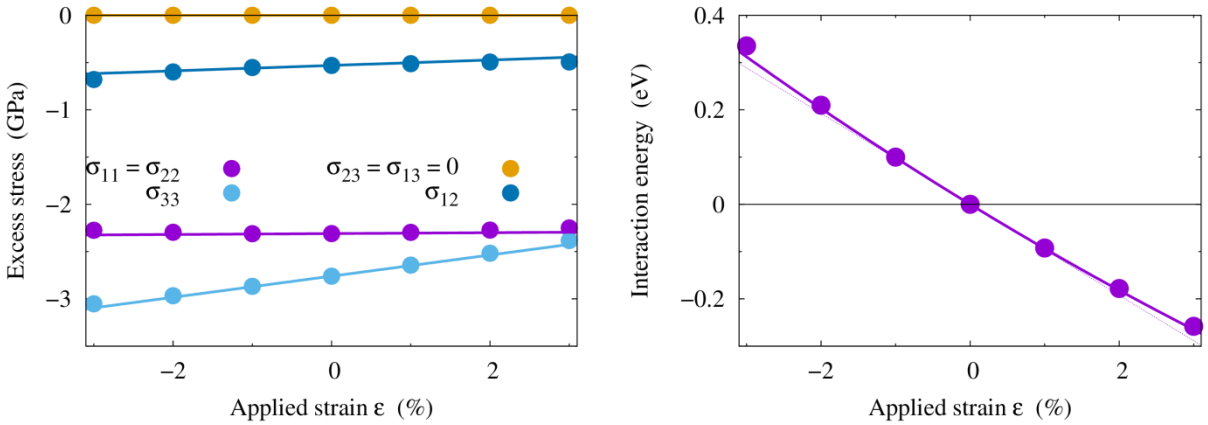


Figure 6: Variation with the shear strain in the (001) plane of the stress (left) and corresponding interaction energy (right) for the vacancy. Symbols are results of ab initio calculations and solid lines of elastic modelling.

- Tetragonal strain along [001]: $\boldsymbol{\varepsilon} = \varepsilon \begin{pmatrix} -1 & 0 & 0 \\ 0 & -1 & 0 \\ 0 & 0 & 2 \end{pmatrix}$

The variations of the non-zero components of the stress tensor are then

$$\Delta\sigma_{11}(\varepsilon) = \Delta\sigma_{22}(\varepsilon) = -\left[P_{11} + (2\alpha_{1133} - \alpha_{1111} - \alpha_{1122})\varepsilon\right]/V$$
$$\Delta\sigma_{33}(\varepsilon) = -\left[P_{33} + (2\alpha_{3333} - 2\alpha_{1133})\varepsilon\right]/V$$
$$\Delta\sigma_{12}(\varepsilon) = -\left[P_{12} + (2\alpha_{3312} - 2\alpha_{1112})\varepsilon\right]/V$$

and the interaction energy

$$E^{\text{inter}}(\varepsilon) = -2(P_{33} - P_{11})\varepsilon - (\alpha_{1111} + 2\alpha_{3333} + \alpha_{1122} - 4\alpha_{1133})\varepsilon^2 .$$

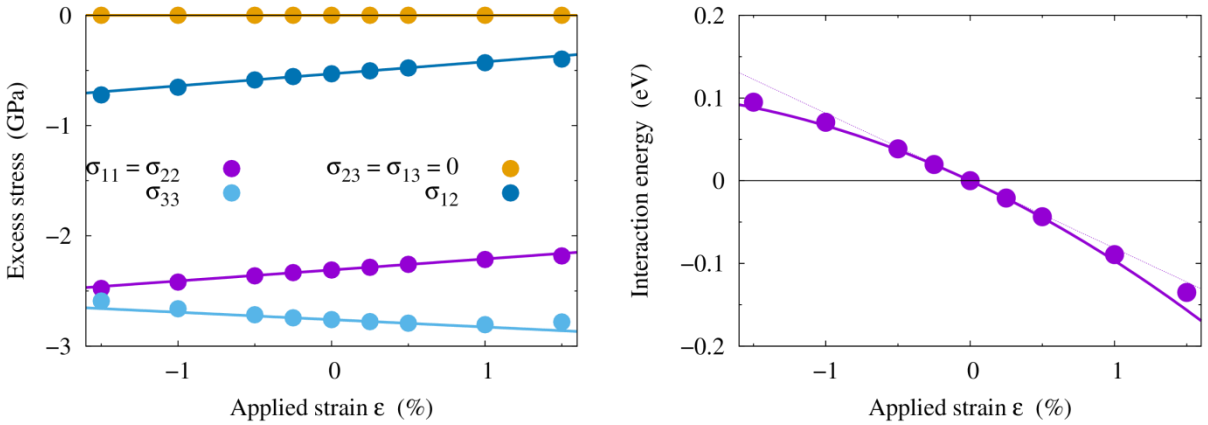


Figure 7: Variation with the tetragonal strain along the [001] direction of the stress (left) and corresponding interaction energy (right) for the vacancy. Symbols are results of ab initio calculations and solid lines of elastic modelling.

- Tetragonal strain along [100]: $\boldsymbol{\varepsilon} = \varepsilon \begin{pmatrix} 2 & 0 & 0 \\ 0 & -1 & 0 \\ 0 & 0 & -1 \end{pmatrix}$

The variations of the non-zero components of the stress tensor are then

$$\Delta\sigma_{11}(\varepsilon) = -\left[P_{11} + (2\alpha_{1111} - \alpha_{1122} - \alpha_{1133})\varepsilon\right]/V$$
$$\Delta\sigma_{22}(\varepsilon) = -\left[P_{11} + (2\alpha_{1122} - \alpha_{1111} - \alpha_{1133})\varepsilon\right]/V$$
$$\Delta\sigma_{33}(\varepsilon) = -\left[P_{33} + (\alpha_{1133} - \alpha_{3333})\varepsilon\right]/V$$
$$\Delta\sigma_{12}(\varepsilon) = -\left[P_{12} + (\alpha_{1112} - \alpha_{3312})\varepsilon\right]/V$$

and the interaction energy

$$E^{\text{inter}}(\varepsilon) = -(P_{11} - P_{33})\varepsilon - \tfrac{1}{2}(5\alpha_{1111} + \alpha_{3333} - 4\alpha_{1122} - 2\alpha_{1133})\varepsilon^2 .$$

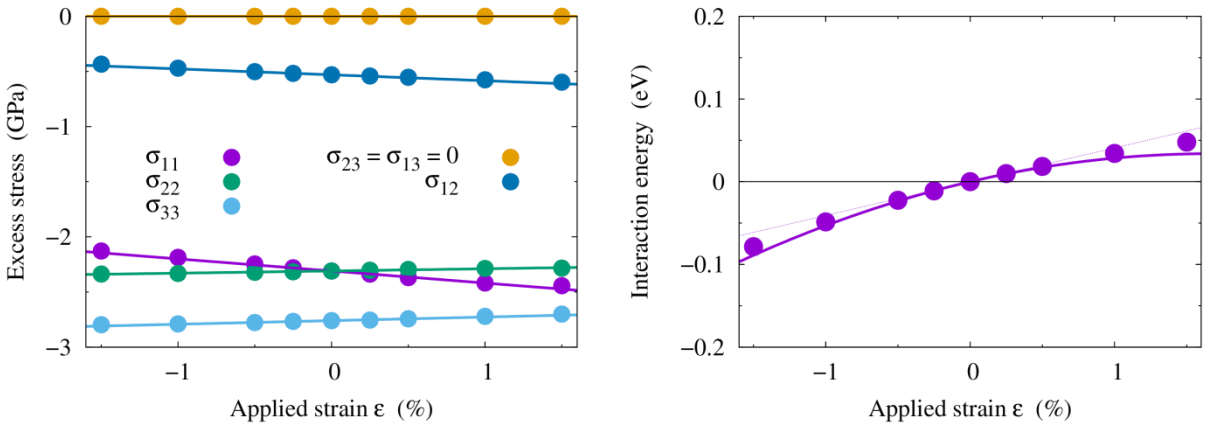

Figure 8: Variation with the tetragonal strain along the [100] direction of the stress (left) and corresponding interaction energy (right) for the vacancy. Symbols are results of ab initio calculations and solid lines of elastic modelling.

The components of the elastic dipole and of the polarizability obtained for the SIA with this approach are given in the table 2 below for ab initio calculations and empirical potentials. Contrary to the vacancy, a strong variability of obtained values for the SIA is observed between the empirical potential. Looking more precisely to the potential Dudarev05, which is used for the atomistic simulations of bias calculations in the next section, this potential underestimates the linear contribution of the SIA interaction with an applied strain (elastic dipole) and overestimates the quadratic contribution (polarizability).

| | | VASP | Marinica 07 | Mendelev 03 | Ackland 04 | Dudarev 05 | Chiesa 09 |
|---|---|---|---|---|---|---|---|
| Form. energy | $E^f$ (eV) | 4.065 | 3.684 | 3.516 | 3.531 | 3.652 | 4.245 |
| Elastic dipole | $P_{11}$ (eV) | 20.93 | 17.32 | 14.63 | 15.00 | 4.37 | 16.65 |
| | $P_{33}$ (eV) | 25.01 | 22.95 | 17.81 | 18.18 | 8.04 | 19.18 |
| | $P_{12}$ (eV) | 4.81 | 6.19 | 3.78 | 3.72 | 8.43 | 4.69 |
| Relax. volume | $\Delta V$ ($\Omega$) | 1.6 | 1.5 | 1.2 | 1.4 | 0.43 | 1.4 |
| Polarizability | $\alpha_{1111}$ (eV) | 8 | -5.71 | 27 | 15 | -196 | -83.16 |
| | $\alpha_{3333}$ (eV) | -2 | 138 | -25 | -30 | -204 | -128 |
| | $\alpha_{1122}$ (eV) | -31 | -83 | -30 | -40 | -22 | -53 |
| | $\alpha_{1133}$ (eV) | -57 ± 5 | -83 ± 3 | 1.4 ± 1 | -15 ± 2 | 8 ± 1 | -31 ± 1 |
| | $\alpha_{1313}$ (eV) | -18 | 27 | 82 | 73 | 72 | 52 |
| | $\alpha_{1212}$ (eV) | -13 | 4 | 41 | 34 | -11 | 11 |
| | $\alpha_{1112}$ (eV) | -2 | -38 ± 3 | -23 ± 3 | -25 ± 2 | 1 ± 4 | -8 ± 2 |
| | $\alpha_{3312}$ (eV) | -52 ± 1 | -57 ± 3 | -41 ± 2 | -42 ± 2 | -47 ± 4 | -36 ± 2 |
| | $\alpha_{1323}$ (eV) | -3 ± 1 | -8 | -18 | -24 | -23 | -21 |

Table 2: SIA properties obtained from ab initio calculations (VASP) and various empirical potentials: formation energy, elastic dipole, relaxation volume and polarizability.

# 4 References for section 1


1 D. J. Bacon, D. M. Barnett, R. O. Scattergood, *Anisotropic continuum theory of lattice defects*, Prog. Mater. Sci. **23** (1980) 51–262.

2 R. Siems, *Mechanical interactions of point defects*, Phys. Status Solidi **30** (1968) 645–658.

3 G. Leibfried, N. Breuer, *Point Defects in Metals I*, Vol. 81 of Springer Tracts in Modern Physics, Springer-Verlag, Berlin, 1978.

4 C. Teodosiu, *Elastic Models of Crystal Defects*, Springer-Verlag, Berlin, 1982.

5. J. D. Eshelby, *The determination of the elastic field of an ellipsoidal inclusion, and related problems*, Proc. Roy. Soc. Lond. A **241** (1957) 376–396.

6. J. D. Eshelby, *The elastic field outside an ellipsoidal inclusion*, Proc. Roy. Soc. Lond. A **252** (1959) 561–569.

7. E. Kröner, *Dia- and para-elasticity*, in: F. Kroupa (Ed.), *Theory of crystal defects*, Academia, 1964, pp. 215–230.

8. H. R. Schober, *Polarizabilities of point defects in metals*, J. Nucl. Mater. **126** (1984) 220–225.

9. M. P. Puls, C. H. Woo, *Diaelastic polarizabilities due to vacancies and interstitials in metals*, J. Nucl. Mater. **139** (1986) 48–59.

10. V. Borodin, J.-C. Chen, M. Sauzay, P. Vladimirov, *Analysis and assessment of mechanisms of irradiation creep*, MATISSE deliverable D2.41 (2016).
11. A. S. Nowick, B. S. Berry, *Anelastic Relaxation in Crystalline Solids*, Academic Press, New York, 1972.
12. J. L. Snoek, *Effect of small quantities of carbon and nitrogen on the elastic and plastic properties of iron*, Physica 8 (1941) 711–733.
13. G. Kresse and J. Furthmüller, Comput. Mater. Sci. **6**, 15 (1996).
14. J. P. Perdew, K. Burke, and M. Ernzerhof, Phys. Rev. Lett. **77**, 3865 (1996).
15. L. Malerba, M. Marinica *et al.*, *Comparison of empirical interatomic potentials for iron applied to radiation damage studies*, J. Nucl. Mater. **406**, 19 (2010).
16. M.-C. Marinica, F. Willaime and J.-P. Crocombette, *Irradiation-Induced Formation of Nanocrystallites with C15 Laves Phase Structure in bcc Iron*, Phys. Rev. Lett. **108**, 025501 (2012).
17. Mendelev, M. I.; Han, S.; Srolovitz, D. J.; Ackland, G. J.; Sun, D. Y. and Asta, M., *Development of New Interatomic Potentials Appropriate for Crystalline and Liquid Iron,* Philos. Mag., 2003 , **83** , 3977-3994
18. Ackland, G. J.; Mendelev, M. I.; Srolovitz, D. J.; Han, S. & Barashev, A. V., *Development of an Interatomic Potential for Phosphorus Impurities in α-Iron,* J. Phys.: Condens. Matter, 2004 , **16** , S2629-S2642
19. S. L. Dudarev and P. M. Derlet, *A 'Magnetic' Interatomic Potential for Molecular Dynamics Simulations*, J. Phys.: Condens. Matter **17**, 7097 (2005).
20. S. Chiesa, P. M. Derlet and S. L. Dudarev, *Free energy of a 10⟩ dumbbell interstitial defect in bcc Fe: Harmonic and anharmonic contributions*, Phys. Rev. B **79**, 214109 (2009).

# 2. Effect of isotropic and shear stresses on dislocation bias factor in bcc iron: an atomistic study

This section describes the work performed at HZDR and SCK and corresponds to the preprint of an article written by A. Bakaev, D. Terentyev, Z. Chang, M. Posselt, P. Olsson and E.E. Zhurkin.

The effect of externally applied stress on the dislocation bias factor in bcc iron has been studied using a combination of atomistic static calculation and finite element integration. Three kinds of dislocations were considered, namely a0/2<111>{110} screw, a0/2<111>{110} edge and a0<100>{001} edge dislocations. The computations reveal that the isotropic crystal expansion leads to an increase or does not change the dislocation bias depending on the Burgers vector and type of the dislocation, while the compressive stress reduces the dislocation bias for all the dislocations studied. The shear stress below Peierls stress causes the decrease of the dislocation bias for edge dislocations and the increase for screw dislocations. Variation of the dislocation bias factor depending on dislocation type and Burgers vector is discussed by analyzing the modification of the interaction energy landscape and the capture efficiency values for the vacancy and self-interstitial atom.

## 1 Introduction

Radiation-induced degradation of the structural steels for nuclear applications is one of the key problems to be studied for ensuring safe exploitation of a large-scale nuclear setup. The present work is devoted to the analysis of the atomistic mechanisms leading to the particular macroscopic effects of neutron radiation, namely: swelling and creep which are the dominating radiation-induced degradation processes in ferritic steels at elevated temperature (i.e. at $T > 0.3 \bullet T_m$, where $T_m$ – is the melting point temperature) [1]. The origin of these phenomena is related to the processes which occur at the nano-scale. During the operation of a reactor the high-energy neutrons penetrate in nuclear materials and cause the atomic displacements which, in turn, lead to the formation of point defects such as vacancies and interstitials. At elevated temperature these defects are mobile and can be absorbed by different sinks. As a matter of fact, any structural steel contains a certain amount of dislocations which are known to be biased sinks for the points defects [2], i.e the dislocations absorb different quantities of interstitials and vacancies (which are always produced simultaneously in the displacement cascades) which can be quantitatively estimated by means of the so called dislocation bias factor (BF).

The experimental assessment of the BF in fcc metallic alloys (Cu, FeCrNi) has already been performed [3, 4] by fitting of the output of the radiation-induced microstructure rate theory model to the experimental analysis of the void swelling upon 1 MeV electron irradiation. The best fit to experimental data was obtained for the BF in the range 0.02-0.04. Another study [5] of the swelling in different fcc-austenitic and bcc-ferritic/martensitc alloys under heavy ions and neutron irradiation revealed the similar swelling rate. Since the swelling rate is proportional to the BF [6], then the BF in bcc ferritic alloys is also of the order of a percent. In the same work [5], the effect of applied stress (hoop stress up to 200 MPa) on the swelling rate in HT9 and 9Cr-1Mo alloys irradiated up to 208 dpa at 400 °C was considered. While for the HT9 steel the swelling was raising from 1 to 3% under application of the stress, no clear correlation was established for the 9Cr-1Mo alloy where the swelling was about 2.5% in both cases, i.e. without and under 200 MPa stress. These findings point to the fact that under different conditions (alloy composition, dislocation density) the stress may or may not have an impact on the dislocation bias, being one of the factors controlling the swelling and irradiation-induced creep phenomena.

The computational assessment of the BF in the stress-free crystals has been performed by Wolfer [7] who applied Ham's solution [8] and isotropic elasticity theory to calculate the BF in fcc Cu which was estimated to be about 0.25 (or 25%). In the more recent studies [9-11] an advanced approach accounting for the anisotropy (found to be important) in the elastic interaction between dislocations and point defects has been applied to calculate the BF in fcc Cu and bcc Fe. Unlike in the work of Morishita [12] where the sink strength of He-vacancy clusters in bcc Fe was estimated by means of the non-explicit approach, i.e. using the total energy of the unrelaxed atomic configurations, the fully explicit method with energy minimization of all atomic configurations to get the dislocation-defect

interaction energy was applied in [11]. In the latter paper the positive BF for the edge dislocations (in the range 0.01-0.06 depending on Burgers vector(BV)) and the negative BF for the screw dislocations (about -0.05) in bcc iron were reported. A possible mechanism of the radiation-induced evolution of the net bias in the crystal was correspondingly proposed: initially the material contains predominantly screw dislocations (characterized by negative BF) while the further irradiation leads to the formation of dislocation loops (being circular- or square-shaped edge dislocations which have a positive BF). It was also noted that the interaction energy (and consequently the BF value itself) between dislocations and self-interstitials or vacancies in the region close to dislocation core differs significantly from the analytical predictions based on the elasticity theory which limits the usage of upper-scale mesoscale methods such as phase field models [13] to evaluate the dislocation sink strength and bias factor. This points to the necessity of performing atomistic simulations of the zone of singularity (i.e. in the vicinity of the dislocation core) in addition to analytical calculations of the outer region. Since different external stresses may modify the stress distribution map in the dislocation core region (and consequently alter the BF value), not only the isotropic stress (inducing the hydrostatic pressure) but also the shear stress being important for nuclear materials applications has to be considered.

The effect of the external stress (shear strain up to ε=0.05%) on dislocation BF in bcc Fe and fcc Cu at *T*=300-500 K has been estimated by means of computer simulations in the paper by Skinner et al. [14]. Interestingly, the negative BF between -0.03 to -0.01 (depending on the applied potential) was calculated for screw dislocation in fcc Cu, which was rationalized as follows: the screw dislocations have a slight bias for vacancies but since it is relatively small, it may be insignificant in the presence of other sinks. For bcc Fe the authors applied the simple pair Johnson potential and considered the <100>-oriented self-interstitials instead of <110> dumbbells, while the latter orientation is the ground state of self-interstitial [15]. Skinner et al. report that for the edge dislocations with the density equal to $10^{14}$ $m^{-2}$ in bcc Fe at *T*=300 K the change of capture efficiency of interstitials and vacancies under application of shear strain up to 0.05% depends significantly on the mutual orientation of the dislocation line and the strain axis. The calculated edge dislocation BF equal to 0.35 in the stress-free crystal was increasing by 0.06 when the stress was applied along the Burgers vector of the dislocation and was decreasing by 0.13 when the stress was acting along the dislocation line. However, for bcc Fe the effect of stress was studied at *T*=300 K only which is too low for modelling the irradiation creep phenomenon. Moreover the application of the external shear stress on the crystals containing a screw dislocation was not studied. Considering the above mentioned drawbacks of this study (including the primitive interatomic potential not accounting for ferromagnetism and the incorrect ground-state configuration of self-interstitials) which lead to the overestimation of the BF even in the stress-free crystal by almost one order of magnitude, there is a need for a new study to account for the contemporary advances in the development of robust interatomic potentials and recently available large computational facilities.

The current work aims to contribute to multiscale modelling of irradiation creep and neutron swelling within the EU project Materials' Innovations for Safe and Sustainable nuclear in Europe (MATISSE) [16] by establishing the reference database of the variation of the BF in bcc iron as a function of material temperature, dislocation type and local stress conditions. The magnitude of the response of BF under the action of either isotropic or shear stress is of interest to parameterize the behavior of representative volume elements in the coarse-grained models, such as standard rate theory method [10, 17, 18]. In this work we continue the study done by Chang et al. [11] introducing external stress in the system of bcc iron with $a_0/2$<111>{110} screw, $a_0/2$<111>{110} or $a_0$<100>{001} edge dislocations. The effects of isotropic expansion and compression up to ±1 GPa and of a shear stress up to 1 GPa on the dislocation BF at the temperatures *T* = 623; 723 and 823 K will be considered. High values of isotropic stress and expansion were selected intentionally in order to catch the amplitude of the bias factor modification and possibly interpolate the result for the lower stresses – relevant for technological applications. The case with the high sensitivity of BF is studied in more detail by means of gradual application of the external load. The results are rationalized on the basis of the analysis of the modification of the interaction energy landscape and the relevant changes of the capture efficiencies of the defects. The special focus is put on a) the off-trend changes (i.e. significant effect of stress on BF) of the BF value under application of isotropic expansion for the $a_0$<100>{001} edge dislocation and b) the BF of screw dislocations under the external stress verifying whether the screw dislocations are characterized by a positive BF (like edge dislocations) under the isotropic (expansive or compressive) or shear stress below Peierls stress.

# 2 Computational details

The details of the numerical method how to calculate the BF were described in details earlier [10, 11]. Here, we will list only the main calculations steps focusing on the differences to the previous studies.

## 2.1 Bias factor

We define the bias factor of a dislocation as:

$$\boldsymbol{B_d} = \frac{\boldsymbol{Z_{SIA}}}{\boldsymbol{Z_{vac}}} - 1, \quad (1)$$

where $Z_{SIA}$ and $Z_{vac}$ are the capture efficiencies of the dislocation for absorption of an SIA or a vacancy, respectively. Following such notation, the positive BF value implies the bias towards the absorption of the interstitials and vice versa. In order to evaluate the capture efficiency Z numerically, we apply the computational approach, proposed by Wolfer [7] which is based on the analysis of the flux of point defects towards the core of a dislocation using the Fick's law with a drift term:

$$\boldsymbol{J} = -\nabla\left(\boldsymbol{DC}\right) - \beta \boldsymbol{DC}\nabla \boldsymbol{E}, \quad (2)$$

where $D$ is the diffusion coefficient, $C$ is the concentration of defects and $\beta$ is equal to $1/k_BT$ where $k_B$ is the Boltzmann constant and $T$ is the temperature, $E$ is the interaction energy between the dislocation and the point defect at a certain point next to it. The Eq. 2 is solved after application of the steady state condition ($\nabla \bullet J=0$):

$$\nabla \cdot \left(-\boldsymbol{e}^{-\beta \boldsymbol{E}} \nabla \Psi\right) = 0, \quad (3)$$

where $\Psi = DCe^{\beta E}$ is the function called diffusion potential. For the solution of the Eq. 3 we applied the following boundary conditions:

a) since the point defects are absorbed [19] within the dislocation core radius (at $r=r_0$), then $\Psi(r_0) = C_1 = 0$. The previously used [9] definition of dislocation core radius based on an interaction energy gradient threshold, was applied in this work. The radius $r_0$ for the particular defect (vacancy or SIA) is defined as the distance from the dislocation where the thermal energy becomes comparable with the gradient of the interaction energy scaled by the Burgers vector, i.e. $b\nabla|E| = k_BT$, where $\boldsymbol{b}$ is the Burgers vector.

b) far from the dislocation (at the dislocation capture range r=R, where the dislocation defect interaction is negligible and the defect concentration C is a constant) the drift term ($\beta DC\nabla E$) is zeroed and the second boundary condition takes the form $\Psi(R) = C_2 = 1$. According to the model used [7], the choice of $C_1$ and $C_2$ constants was arbitrary except for the fact that they should satisfy the condition $C_1 < C_2$ so that the concentration difference drives point defect flow to the center, i.e. to the dislocation core.

The total current of the point defects towards the dislocation can be evaluated as follows:

$$J_{tot} = r_o \int_o^{2\pi} J_r\left(r_0, \theta\right) d\theta, \quad (4)$$

where $r_0$ is the dislocation core radius vector and $J_r(r_0,\vartheta)$ is the current of the point defects towards the core in the certain position. Finally, the capture efficiency of a point defect can be evaluated as: $Z = \frac{J}{J_0}$, where $J_0$ is the flux in the bulk iron (the crystal without a dislocation).

The general strategy of the numerical calculation of the BF following the above mentioned methodology: Firstly, the atomistic simulations are performed to get the interaction energy between dislocation and point defect in the vicinity of the dislocation core, i.e. in the region where the elasticity theory considerations are not sufficient to

describe the interaction in an adequate way. Later on, the interaction energy map is extended outside the zone studied by atomistic simulations up to the desired dislocation density using the analytical prediction of the interaction energy. The final step consists in the numerical integration of the bias factor using the finite element approach following the Eqs. 2-4.

## 2.2 Atomistic calculations towards the construction of the point defect-dislocation interaction energy maps

The calculations were performed using the model of a periodic array of dislocations developed by Osetsky and Bacon [20]. The point defect (self-interstitial or vacancy) was introduced at a certain position nearby the dislocation core and after that the system was relaxed using the molecular static algorithm implemented in the code DYMOKA [21]. Given that here we are interested in the impact of the applied stress, the extended relaxation procedure was applied in order to increase the accuracy of calculations and optimize the speed of crystal relaxation. The combined procedure based on conjugate gradient algorithm and thermal annealing followed by quenching was therefore used.

In order to be consistent with previous investigations [11] the interatomic potential developed by Dudarev and Derlet (case II) [22] for bcc iron was used. Typical dimensions of the simulation cell were 40 x 40 x 4 $nm^3$, where 4 nm is the size along the dislocation line. The total number of iron atoms was about $5 \bullet 10^5$ and the dislocation line density was about $5 \bullet 10^{14}$ $m^{-2}$.

The vacancies were introduced by means of removal of an atom, while interstitials were inserted as two atoms sharing the same lattice site having the orientation <110> and located at the distance of 0.4 $a_0$, centered on a lattice site. There are six non-equivalent <110> orientations of a dumbbell in the crystal and the interaction energy of all of them was averaged to get the final value for an interstitial at a certain point.

Two types of the external stress were separately applied to the crystal prior to the relaxation procedure: isotropic compression or expansion by ±1 GPa and shear stress up to 1 GPa depending on the dislocation type (see Table 1 for details). The Peierls stress reported in the table was calculated using molecular static simulations following the algorithm described in [20, 23, 24]. The isotropic stress was introduced by adjusting the lattice constant so that the external pressure value reaches +1 GPa or -1 GPa for the expansion and compression, respectively. The shear stress was induced by shifting the upper block of atoms so as the desired shear stress acting on the bottom block of atoms in the direction of the applied stress is reached.

The interaction energy between a defect and a dislocation $E_i$ was calculated using the equation [25]:

$$E_i\left(\left\{A_{disl+def}\right\}\right) = \left[E_{total}\left(\left\{A_{disl+def}\right\}\right) + E^0_{total}\right] - \left[E_{total}(A_{disl}) + E_{total}(A_{def})\right], \quad (5)$$

where $E_{total}(A_{disl})$ *and* $E_{total}(A_{def})$ are the total energies of the configuration containing the dislocation and the defect only, respectively, $E_{total}(\{A_{disl+def}\})$ is the total energy of the configuration with the dislocation and the defect, and $E^0_{total}$ refers to a configuration containing no defects, i.e. bulk bcc iron. Following this notation, a negative value implies an attractive interaction and vice versa.

Table 1: The applied shear stress depending on the considered dislocation. The Peierls stress calculated using molecular statics simulations is shown in brackets.

| Dislocation type | Shear strain, % | Shear stress (Peierls stress) |
|---|---|---|
| edge $a_0$<100>{001} | 0.7416 | 1.0 GPa (11.7 GPa) |
| edge $a_0/2$<111>{110} | 0.0359 | 60 MPa (137 MPa) |
| screw $a_0/2$<111>{110} | 1.0925 | 1.0 GPa (5.9 GPa) |

### 2.3 Analytical calculations to extend the interaction energy map

The analytical calculations of the interaction energy, outside the atomistically treated region, were performed following the elastic model described in [10] for edge dislocations and in [11] for screw dislocations.

For the isotropic stress the new lattice constant (updated as described in the previous section) was used for the calculation of the magnitude of Burgers vector in the analytical formulas. For the shear stress, the modification of the analytical calculations was performed by means of introduction of the additionally applied shear strain components ($\varepsilon_{12}$ and $\varepsilon_{21}$, which are equal one to another and are listed in the Table 1) in the strain tensor of the dislocation.

### 2.4 Finite elements calculation of the bias factor

The finite elements approach to evaluate the bias factor does not differ from the previous studies by Chang et al. [10, 11]. Firstly, the interaction energy maps obtained by atomistic molecular statics calculations and the outer-region extension based on the theoretical predictions according to the elasticity theory were merged into a common energy profile. Later on, firstly the MATLAB subroutines were applied to calculate the dislocation core radii for vacancies and interstitials for each of the dislocations and stress types studied. The list of the calculated dislocation core radii is presented in the Table 2. The values were calculated taking 823 K as the ambient temperature (following the methodology in [11]). These data were also used for the studied temperatures of 623 K and 723 K since for this temperature range the $\nabla|E|$ difference is not significant. After that, the numerical solution of the differential equation Eq. 2 using the finite elements method was performed in order to estimate the resulting capture efficiency and finally, to derive the dislocation bias factor value.

Table 2: The dislocation core radii used in this work. The values given in brackets were obtained from analytically calculated interaction energy maps.

| | Dislocation core radius, Å | | | | | |
|---|---|---|---|---|---|---|
| Dislocation type | Compression (1 GPa) | | No stress | | Expansion (1 GPa) | |
| | SIA | Vac | SIA | Vac | SIA | Vac |
| edge $a_0$<100>{001} | 13 | 10 | 13 (9) | 11 (6) | 14 | 10 |
| edge $a_0/2$<111>{110} | 12 | 10 | 12 (8) | 10 (5) | 13 | 10 |
| screw $a_0/2$<111>{110} | 8 | 6 | 8 (5) | 6 (3) | 8 | 6 |
| | Shear stress | | | | | |
| edge $a_0$<100>{001} | 13 | 11 | | | | |
| edge $a_0/2$<111>{110} | 12 | 10 | | | | |
| screw $a_0/2$<111>{110} | 8 | 6 | | | | |

## 3 Results and discussion

### 3.1 Effect of stress on point defects and dislocations

Prior to study of the effect of stress on the crystals containing both defects, i.e. the dislocation and the point defect (SIA or vacancy) simultaneously, we have studied the effect of stress on the core structure of dislocations and the dilatation volume of point defects separately.

The effect of isotropic expansion or compression up to 1 GPa and shear stress (1 GPa for BV=<100> and 60 MPa for BV=½<111>) on the core structure of the edge dislocation is shown on Fig. 1. The relative displacement (in units of BV) of atoms constituting the two planes bounded the imaginary dislocation glide plane is presented. The relative displacement has a meaning of Burgers vector density, as the total displacement amounts to the value of the Burgers vector. A positive displacement implies compression, negative – tension. Naturally, for both dislocation types studied i.e. with BV=<100> and BV=½<111>, the atoms in the upper layer get close to each other (the positive relative displacement) in the compressive regions (Fig. 1a and 1b) and vice versa in the lower layer in the tensile regions (Fig. 1c and 1d).

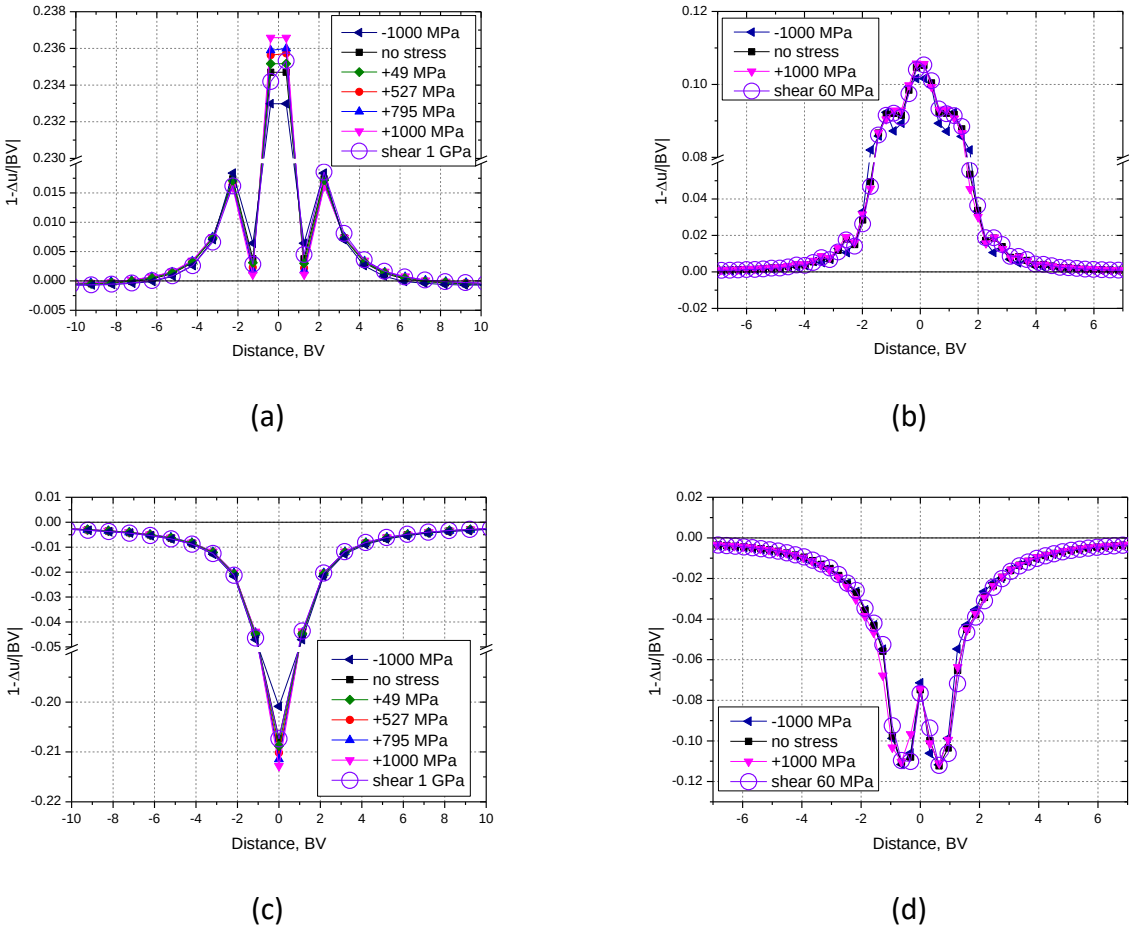


Fig. 1: The relative displacements (in units of Burgers vector ***b***) of atomic layers above (upper layer) and below (lower layer) the edge dislocation core. The figures a) and b) correspond to the upper layers, while c) and d) to the lower layers. The edge dislocation with BV=<100> is shown in a) and c), while b) and d) correspond to the edge dislocation with BV=½<111>.

Such oversized defects as SIAs prefer the tensile regions (lower layer and below), while the vacancies (undersized defects) migrate to the compressive regions (upper layer and above) to minimize the cumulative lattice strain. The upper dislocation atomic layer of the edge dislocation with BV=½<111> (Fig. 1b) and the bottom layer of the one with BV=<100> (Fig. 1c) are compact meaning that vacancies and SIAs, respectively, will prefer to occupy the

central position (i.e. the dislocation core itself) and the attraction will decrease monotonically with a distance from the dislocation core. Interacting with the edge dislocation with BV=<100> the vacancies will tend to occupy the central position and another position at the distance of 2.2·BV from the dislocation core (as shown in Fig. 1a) while the interaction energy should be low at the distance of 1.3·BV. Approaching the core of the edge dislocation with BV=½<111> the SIAs will tend not to occupy the central position itself but rather the lower-energy positions at the distance of (0.6-1.0)·BV from the dislocation. As one can see, these anticipations remain valid for the stress-free conditions and both isotropic and shear stresses. The application of the external load leads to the negligible change of the relative displacement of the atoms nearby the dislocation core and no modification of core structure is observed. Thus, no significant change of the interaction energy maps for SIAs and vacancies next to the edge dislocations due to the effect of stress on dislocations only can be expected under the application of isotropic (below 1 GPa) or shear load below Peierls stress.

In order to estimate the effect of stress on point defect properties we have evaluated the relative change of dilatation volume for SIAs and vacancies under the isotropic expansion or compression up to 1 GPa and the results are summarized in the Fig. 2. As one can see, although the isotropic expansion or compression up to 300 MPa affects the dilation volume of both defects, decreasing or increasing this volume, respectively, this change is nearly the same for vacancies and SIAs leading to no modification of the bias factor value (see Eq. 1) within this stress range. Further increase of any kind of isotropic load leads to the faster deviation of the dilatation volume of vacancies compared to SIAs from the zero-pressure value. In this case since the interaction energy between point defects and dislocations is proportional to the dilation volume [10], the application of isotropic compressive or expansive load will lead to the faster increase or decrease, respectively, of interaction energy of vacancies, compared to SIAs. Naturally, the increase of capture efficiency of dislocations should correlate with the increase of the interaction energy. According to the Eq. 1, the faster increase of capture efficiency of vacancies compared to SIAs during the isotropic compression leads to the decrease of bias factor and vice versa for the isotropic expansion. Note, that since the shear stress has no impact on the dilatation volume and dislocation core structure, one can expect no (or very little) effect of such stress on the bias factor value.

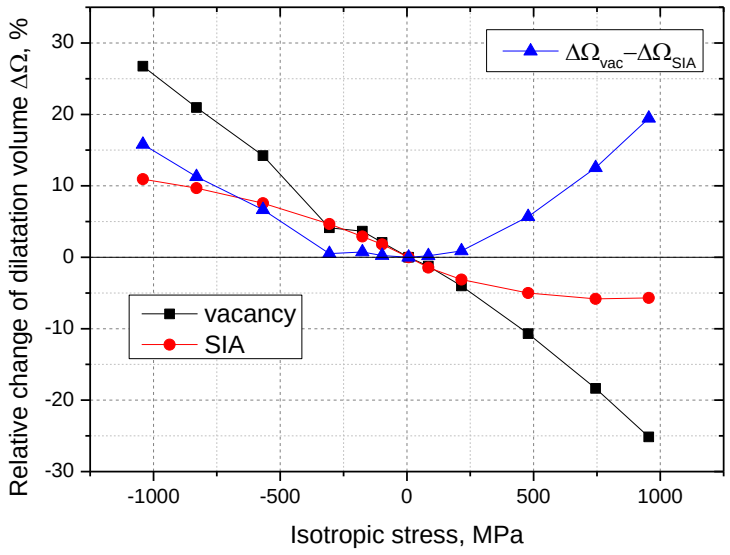


Fig. 2 – The relative change of dilatation volume for vacancies and SIAs under the isotropic expansive or compressive load up to 1 GPa. Positive values of stress correspond to the isotropic expansion. The difference between the relative change of relaxation volume for vacancies and SIAs is also demonstrated.

### 3.2 Stress-free calculations

We have redone the stress-free bias factor calculations of Chang et al. [11] for the three dislocations, using the analytical elasticity theory considerations and the finite element method implying the optimized numerical procedures, thus improving the accuracy of the results. Also, we have redone the stress-free atomistic calculations of the BF previously executed by Chang et al. [11] applying the extended relaxation procedure for the crystals as it was described in section 2.2. The new atomistic interaction energy maps for three dislocations with SIAs or vacancies are presented in the left columns of the Fig. 8 and Fig 9, respectively. One can see, that compared to the results in [11] the atomistic interaction energy landscape became more symmetrical (mirror symmetry along [111] with respect to the dislocation core position) for the edge dislocation with BV=½<111>. Nevertheless, the atomistic dislocation bias factor value (shown in Fig. 3) of 0.055 is very close to the value of 0.060 obtained in [11]. For the edge dislocation with BV=<100> compared to results in [11] the bias factor has dropped by 0.015 for all the temperatures considered and became negligibly small at 723 and 823 K. Interestingly, that unlike in [11] we have found that the analytically calculated bias factor of the edge dislocation with BV=<100> is lower than the one of the edge dislocation with BV=½<111>. Intuitively, the opposite would be expected (see discussion in [11]). The obtained result implies that both our atomistic and fully analytical calculations of bias factor contradict with the early assumption that the BF value should be proportional to the modulus of the BV [26]. Note that in the experiment by Katoh et al. [27], no clear correlation between the density of dislocations with a particular BV (<100> or ½<111>) and the measured swelling was established.

Here, we also report the analytical and atomistic values of dislocation bias factor for the screw dislocation which was not presented yet by Chang et al. [11]. Although the analytical predictions point to the very small positive bias factor value (below 0.01), the atomistic simulations show the negative bias factor of about -0.06 (i.e. preferential absorption of vacancies compared to interstitials). The physical model for void swelling in bcc metals which considers the negative bias factor for screw dislocations was discussed in [11].

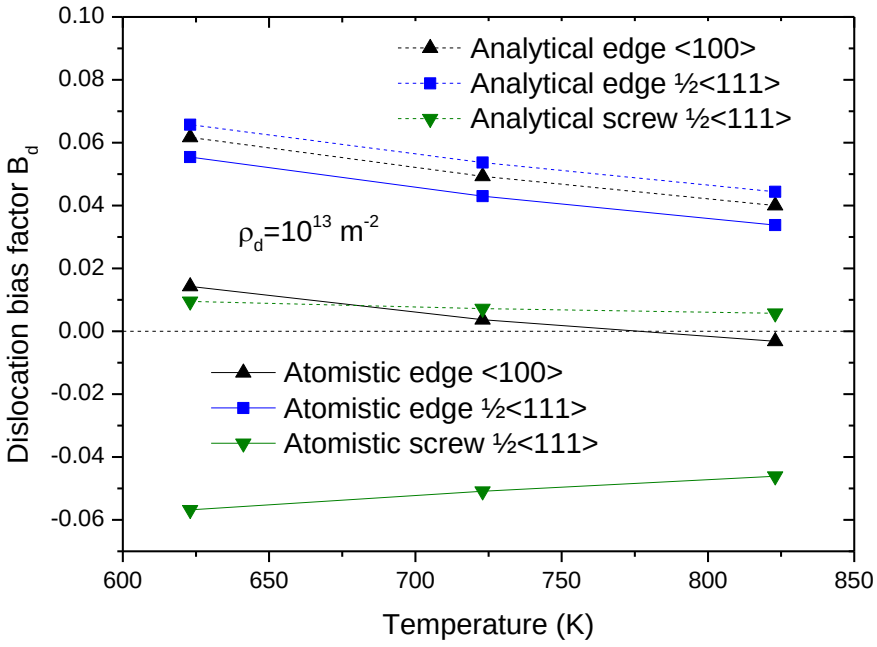


Fig. 3 – The dislocation bias factor of two edge and one screw dislocation calculated using atomistic simulations and analytical calculations. The external stress is equal to zero.

### 3.3 Bias factor under isotropic stress

The application of external stress has an effect on the interaction energy landscape. The corresponding modifications are presented on Fig 4. The application of lattice units (LU) on horizontal and vertical axes allows one to analyze the difference between the interaction landscape in two crystals: with and without stress applied. One can see that the interaction energy in a zone with a radius up to 1 nm (~3 LU) is affected. The patterns in Fig.4 differ significantly depending on the dislocation and point defect type. The common trend points that the compression reduces the interaction strength for SIAs and enhances it for a vacancy. The opposite is found for expansion. This atomistic findings point to the synergistic effect of interaction of edge dislocations with point defects since the increase of interaction energy (and of the capture efficiency) for both SIAs and vacancies was expected (see Section 3.1) for the isotropic compression and vice versa for the expansion.

The exact location of the zones with an increased attraction is easy to explain for the edge dislocations which were created by means of insertion of the extra plane. The positive pressure makes even more favorable for a vacancy to stay in the compressed (upper layers) region of the dislocation core. For SIAs the negative pressure makes more favorable the allocation of them in the tensile region (lower layers) of the dislocation core. One can also note the two separated zones of the large change of the interaction energy for SIAs and both types of edge dislocations (especially for <100> dislocation), while the zone of change is far more compact for the vacancies. The stress-induced shift of the interaction energy map for the screw dislocation is also remarkable. For SIAs the maximum shift was not in the center of the dislocation core but in the ring with radius 3-7 Å centered on the core. The compression leads to the decrease of the attraction in this ring and vice versa for the expansion. The similar modification is captured for vacancies located next to the screw dislocation: while the triangular-shaped zone with an outer radius of 3 Å is not affected by the isotropic load, the interaction energy in the outer region is evenly decreasing under compression and increasing under expansion. One can also note the magnitude of the change of the interaction energy between point defects and a dislocation is almost by one order of magnitude smaller (mind the color code scales) for the edge dislocations compared to screw dislocation under the equivalent loading conditions.

Since there is a modification of the interaction energy maps, the external stress has also an effect on the capture efficiency of the point defects by dislocations. The relative change of the capture efficiency lies in the range from -2% to +3% with the only exception for the edge dislocation with BV=<100> and SIA where the capture efficiency was raising by 6.1%. The latter case will be discussed in details later. Interestingly, the expansive load leads to a certain increase of the capture efficiency independently on dislocation type, its BV and defect type, while the compressive load leads to a decrease of it for screw dislocations whereas both an increase and a decrease are found for the edge dislocations.

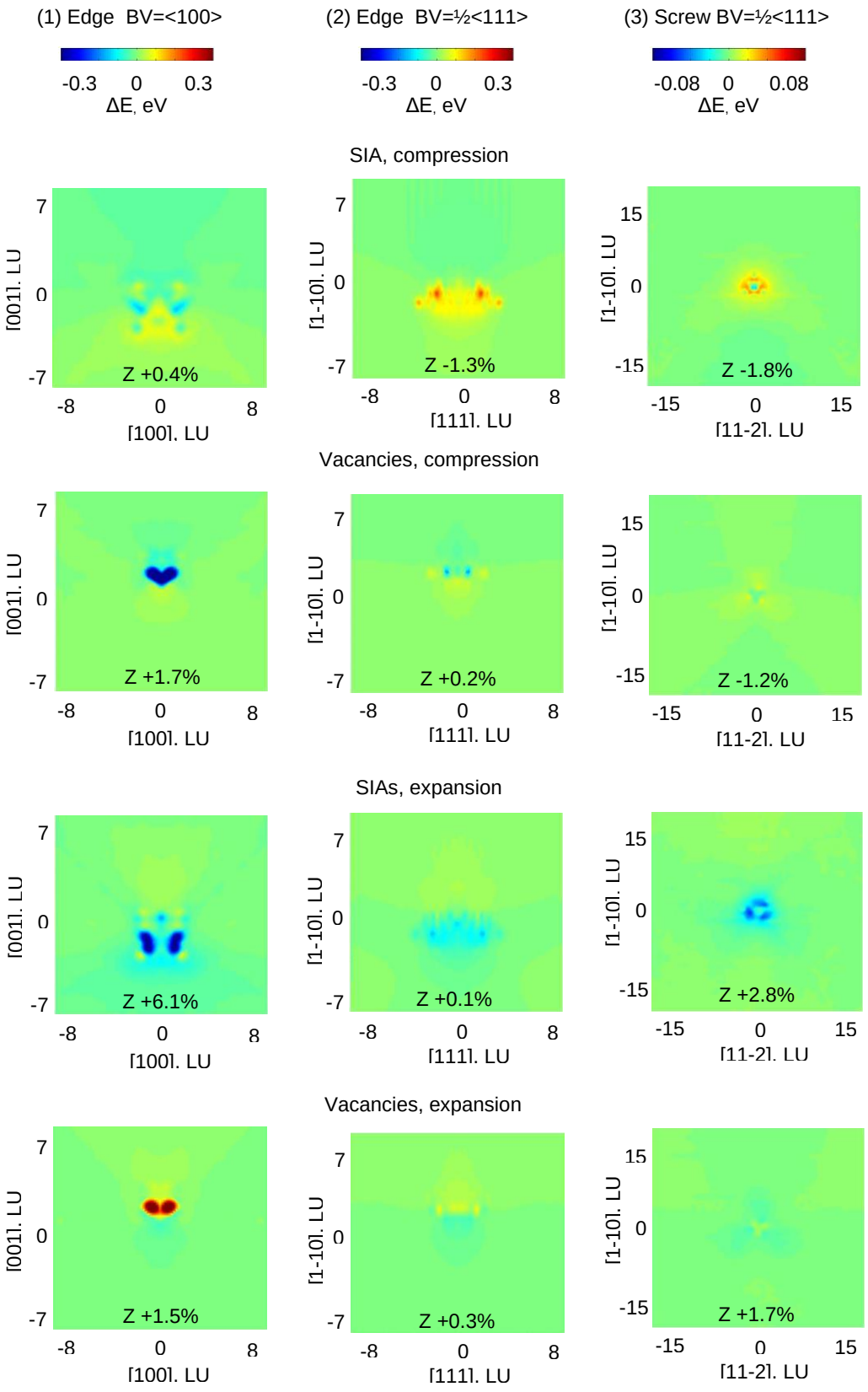


Fig. 4 – The absolute difference between the dislocation-defect interaction energy computed under isotropic compression (1 GPa) or expansion (1 GPa) and in the unloaded crystals. The negative values correspond to the increase of the interaction energy. The corresponding relative change of the capture efficiency of the defect by the dislocation is also shown in the figure. The type of the dislocation and its Burgers vector is specified on the top of each column.

The dislocation bias factor under the isotropic stress in comparison with the stress-free case is presented in Fig. 5. One can see that the isotropic compression (see Fig. 5a) leads to the decrease of the bias factor for all the dislocations studied, which correlates well with our estimations based on the separate analysis of the effect of stress on point defects and dislocations discussed in the Section 3.1. The change for edge dislocation is three times stronger than the one for the screw dislocation. Note, that the dislocation bias practically disappears for the dislocation with BV=<100> at 623 K and reverses from preferential absorption of interstitials to vacancies at 723 K and above. The magnitude of the latter effect is very small to cause any effect on the evolution of the radiation damage in the material since the absolute value of the bias factor in this case is very close to zero. For the edge dislocation with BV=½<111> the isotropic compression leads to the clear decrease of the preferential absorption of SIAs and to the increase of the preferential absorption of vacancies for a screw dislocation with the same BV. Similarly to the case of isotropic compression, the effect of isotropic expansion (see Fig. 5b) is significantly dependent on both dislocation type and magnitude of BV. Initially, in the Section 3.1 we anticipated that the bias of edge dislocation will increase under the expansive load. The atomistic simulations and the finite elements integration have shown that the bias of the edge dislocation with BV=½<111> was not affected by the action of the expansive load. Contrariwise, the bias factor of the edge dislocation with BV=<100> has increased significantly up to 0.06 (at 623 K). The bias factor of the screw dislocation with BV=½<111> was decreasing by 0.01, thus diminishing the preferential absorption of vacancies.

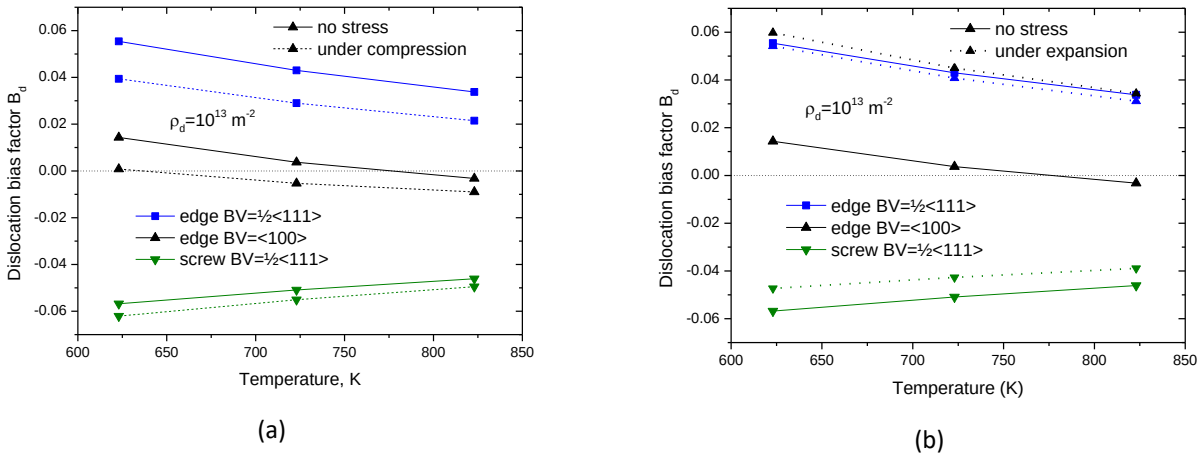


Fig. 5 – The dislocation bias factor of three dislocations studied under (a) isotropic compression (1 GPa) and (b) isotropic expansion (1 GPa).

As was described above, the large change of the bias factor for the edge dislocation with BV=<100> was caused mainly by the significant increase of the capture efficiency of SIAs by 6.1% (assisted by the moderate increase of the capture efficiency of vacancies by 1.5%). In order to analyze better this phenomenon we have performed additional atomistic simulations introducing the isotropic expansion of a smaller magnitude, i.e. 49, 129, 261, 527 and 795 MPa. The new interaction energy landscapes for the SIAs for three intermediate expansive stresses of 49, 527 and 795 MPa are presented in Fig 6. One can observe the anisotropic modification of the region next to the dislocation core under the gradual increase of the magnitude of the load. While the relatively low stress of 49 MPa leads only to a decrease of the interaction energy for SIAs next to the dislocation core, a higher applied stress (of 527 and 795 MPa) leads to the heterogeneous modification of the interaction energy pattern: three compact zones appear where the attraction increases by 0.4 eV (or higher) and four compact zones where the attraction decreases. The interaction energy map of the crystal under the highest stress which was studied here, i.e. 1 GPa (see Fig. 4)

is characterized by the significant enlargement of the four zones with the increase of the interaction energy and a reduction of the zones with the decrease of it, which, as a result, leads to the significant increase of the capture efficiency by 6.1% compared to the stress-free case.

After that we analyzed the change of the capture efficiencies of SIAs and vacancies and of bias factor, which are shown in Fig. 7a and 7b respectively. We have identified three ranges of stress that lead to a different effect on capture efficiency and the bias factor:

I. Low stress zone (below 50 MPa). The application of this relatively small stress leads to the immediate increase of capture efficiencies of SIAs by 2.2% and of vacancies by 0.7%. The corresponding bias factor rises from 0.015 (without stress) up to 0.030.

II. Intermediate regime (50-700 MPa). The further application of the external expansive stress does not lead to a modification of the capture efficiency as compared to the previous regime. The bias factor value stays in the range 0.030-0.035.

III. High stress zone (above 700 MPa). The regime is characterized by the pronounceable changes of capture efficiencies of SIAs and vacancies while application of the increased stress. Unlike in the regimes I and II, the dislocation core radii change for both vacancies (decreases by 1 nm) and interstitials (goes up by 1 nm). The raise of capture efficiency of SIAs while increasing the stress from 800 MPa to 1 GPa is very large, i.e. 4%. Correspondingly, the BF raises from 0.01 to about 0.06.

In the Fig. 2 one can see that the dilation volume (and consequently the interaction energy and the capture efficiency) for SIAs tends to saturate at the expansive stress of 250-300 MPa and above, while the dilatation volume of the vacancy keeps decreasing monotonically with the additional expansive load. Since the results our atomistic simulations of the interaction of point defects and vacancies do not match the estimations based on the separate effect of stress on point defects and dislocations, this can indicate to the presence of the synergistic effect being an intrinsic feature of the atomistic model applied in this work.

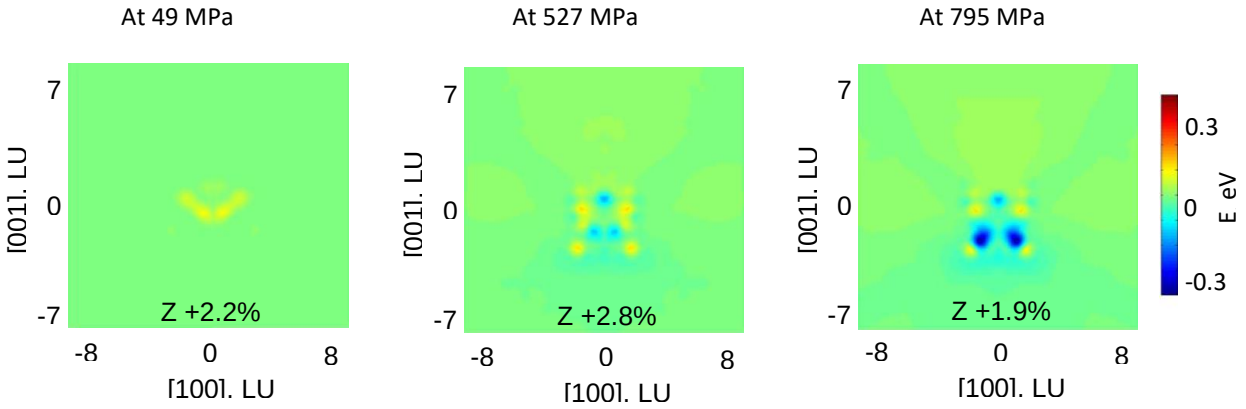


Fig. 6 – The absolute difference between interaction energy of edge dislocation with BV=<100> and SIAs without an external stress and under gradual isotropic expansion. The negative values correspond to the increase of the interaction energy. The corresponding relative change of the capture efficiency of the defect by the dislocation is also shown in the figure.

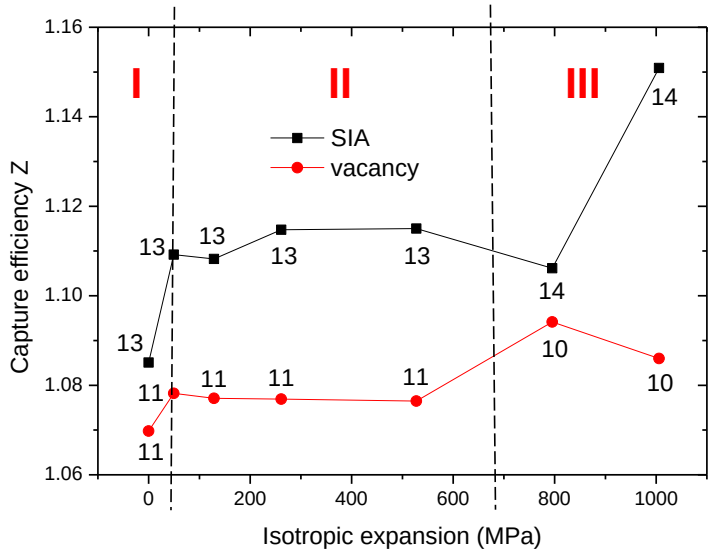


(a)

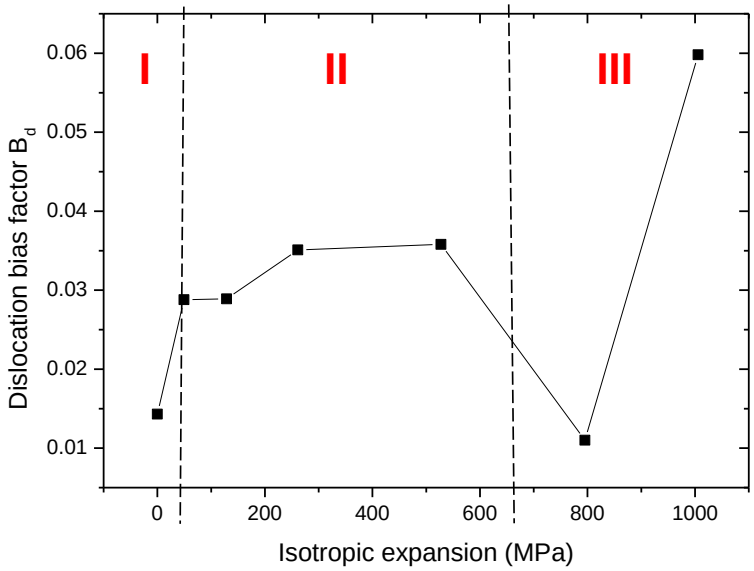


(b)

Fig. 7 – a) The capture efficiencies of SIAs and vacancies and b) dislocation bias factor of the edge dislocation with BV=<100> under gradual isotropic expansion. The dislocation core radii used for the calculation of the capture efficiencies of point defects are shown in a).

### 3.4 BF under shear stress

We have analyzed the modification of the interaction energy landscape under application of the external shear stress and the relevant modification of capture efficiencies (see Fig. 8 for SIAs and Fig.9 for vacancies). Unlike the expected absence of the effect of shear stress (see discussion in Section 3.1), the atomistic simulations have shown that the application of external shear stress leads to a certain change especially in the nearest vicinity of the dislocation core and this change is more pronounced for SIAs compared to vacancies. We have noted the effect of the different Burgers vectors for edge dislocations: the

smaller BV=½<111> leads to the decrease of capture efficiency for SIAs and vacancies while the larger BV=<100> leads to the increase of it. Since the shear stress was different for these dislocations, this effect might also be attributed to the magnitude of the applied stress. The overall effect of the application of the external stress is the anisotropic modification of the interaction energy in the region of 10-15 Å around to the dislocation core and a consequent change of the capture efficiency in the range from -2.2 to +0.7 %.

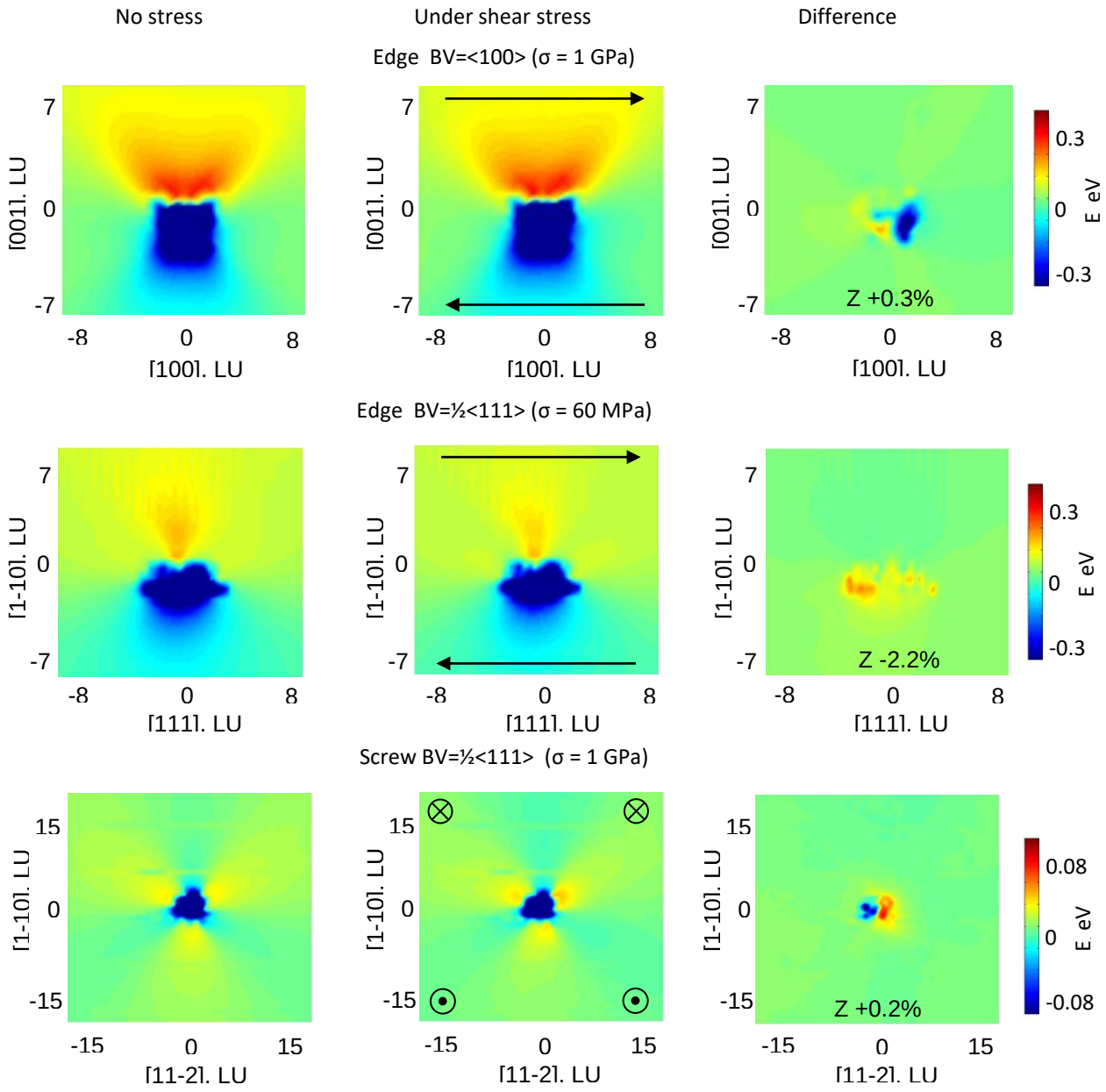


Fig. 8 – Interaction energy maps for SIA around dislocations before application of external stress, under shear stress σ and the corresponding absolute difference. For the latter case the negative values correspond to the increase of the interaction energy. The relative change of the capture efficiency of the defect by the dislocation is also shown in the figure.

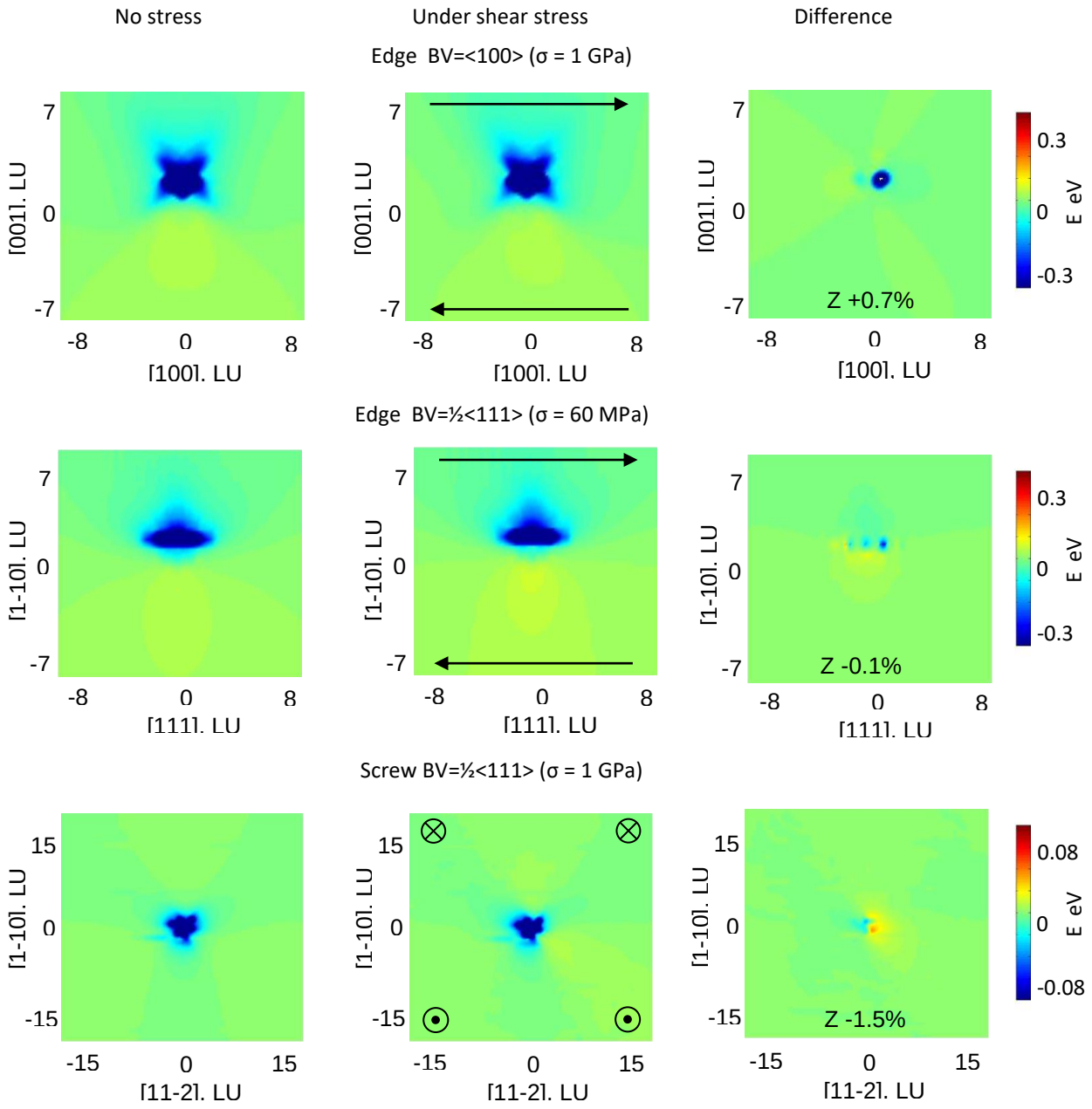


Fig. 9 – Interaction energy maps for vacancies around dislocations before application of external stress, under shear stress σ and the corresponding absolute difference. For the latter case the negative values correspond to the increase of the interaction energy. The relative change of the capture efficiency of the defect by the dislocation is also shown in the figure.

The dislocation bias factor for the studied dislocations under the application of external shear stress in comparison with stress-free crystal is shown in Fig. 10. One can see that for screw and edge dislocations with BV=½<111> the application of the shear stress of 1 GPa (60 MPa for edge dislocation), leads to the relative decrease of the dislocation bias factor by about 40%, namely by 0.020 down to 0.035 for the edge and by 0.02 up to -0.04 for the screw dislocations at *T*=623 K. The edge dislocation with large BV=<100> was almost unaffected by the application of shear stress of 1 GPa: the BF was decreasing by less than 0.005.

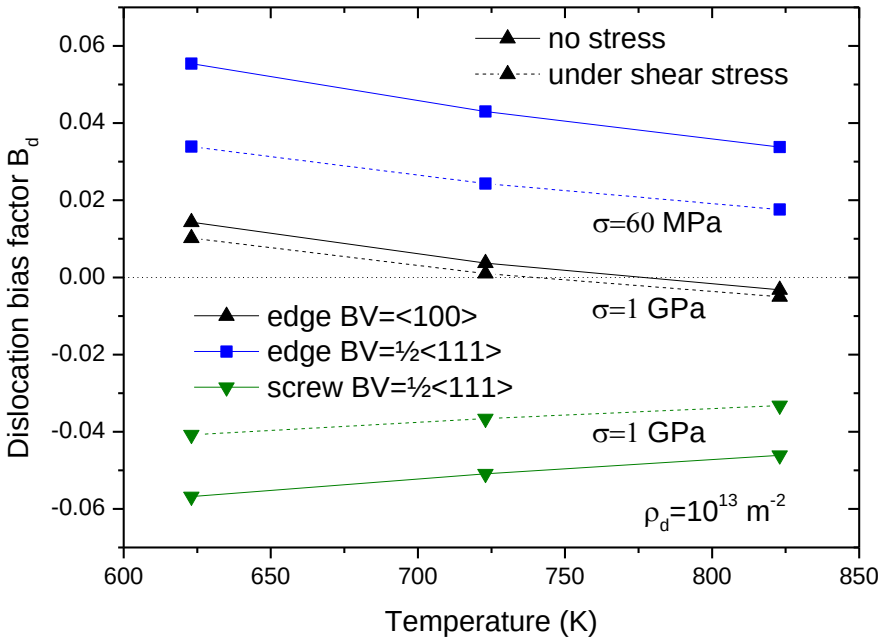


Fig. 10 – The dislocation bias factor of three dislocations studied under shear stress σ (60 MPa – 1 GPa).

## 4. Summary and conclusions

In this work we have performed the computational assessment of the dislocation bias factor in bcc iron with $a_0/2$<111>{110} screw, $a_0/2$<111>{110} or $a_0$<100>{001} edge dislocations under the application of the external isotropic (compressive and expansive) and shear stress below Peierls stress. Prior to the study of the interaction of dislocations and points defects, the separate analysis of them (dislocation core structure and dilatation volume calculation) was done in order to anticipate the effect of stress on the bias factor value. The increase of bias factor under the isotropic expansion, vice versa for the compressive load and no change of bias factor for the shear load were expected. After that the combination of atomistic simulations and finite elements calculations was applied in order to derive the dislocation bias factor, i.e. quantify the preferential absorption of self-interstitials or vacancies. On the basis of the results obtained we can draw the following conclusions:

1) Isotropic compression of 1 GPa leads to a decrease of bias factor by 0.01-0.02, while the expansion of 1 GPa leads to an increase up to 0.045. Since the bias factor of the screw dislocation in the crystal without any stress is negative, the compression leads to the increase of the bias towards vacancies and vice versa in case of the expansive stress. The reason for the change of the bias factor value is related to the anisotropic modification of the interaction energy landscape concentrated in the region within 1 nm from the dislocation core. The gradual increase of the applied isotropic expansion in the range 50 MPa  1 GPa has shown the non-linear change of the capture efficiency of SIAs and vacancies, and the corresponding dislocation bias factor values for the edge dislocation with BV=<100>. Such changes were rationalized on the basis of the particular modification of the pattern of the interaction energy map.

2) The applied shear stress (below Peierls stress: 60 MPa for edge dislocation with BV=½<111> and 1 GPa for the other two dislocations) leads to the relative reduction of the dislocation bias for all the studied dislocations by about 40%, namely the decrease of bias factor by 0.02 for the edge dislocations and the increase of bias factor by 0.02 for the screw dislocations. The origin of the effect is explained by the anisotropic modification of the interaction energy landscape in the core region within 10-15 Å, predominantly for the SIAs.

3) The modification of the interaction energy map after the application of isotropic or shear stress was deviating in many cases from our estimations based on the effect of stress on the dislocation or the point defects separately due to lattice strain relief. This finding points to the presence of the synergistic effect of the interaction of dislocations and the point defects being the intrinsic feature of the atomistic model applied in this work.

4) The application of the external isotropic and shear stress does not change the negative sign of bias factor for the ½<111> screw dislocation obtained earlier.

5) The revealed effect of isotropic or shear stress on dislocation bias factor does not introduce any cardinal changes of its value compared to the stress-free case. Therefore, the hypothesis of Chang et al. [11] about the evolution of radiation damage, i.e. emergence of void swelling at a certain dose when the large enough population of edge dislocations (dislocation loops) appears in the material which unlike screw dislocations are characterized by the positive bias factor, remains relevant. However, the confirmation of this hypothesis requires further investigation.

The obtained parameters of dislocation bias factor as a function of material temperature, dislocation type and local stress conditions are planned to be used as reference database for the upper scale models, such as standard rate theory method [10, 17, 18], for the modelling of evolution of radiation damage accounting for void swelling and irradiation creep in Fe-based alloys, including ferritic-martensitic steels, in the unloaded state or under the external isotropic or shear load.

# 5 References for section 2

[1] G.S. Was, *Fundamentals of Radiation Materials Science: Metals and Alloys*, Springer, 2007.

[2] G. Greenwood, A. Foreman and D. Rimmer, J. Nucl. Mater. 4 **(**1959) 305-324.

[3] S.I. Golubov, B.N. Singh and H. Trinkaus, Philosophical Magazine A 81 **(**2001) 2533-2552.

[4] G.P. Walters, J. Nucl. Mater. 136 **(**1985) 263-279.

[5] F.A. Garner, M.B. Toloczko and B.H. Sencer, J. Nucl. Mater. 276 **(**2000) 123-142.

[6] J.J. Sniegowski and W.G. Wolfer 1984 Proceedings of the Topical Conference on Ferritic Alloys for use in Nuclear Energy Technologies, AIME pp. 579-586.

[7] W.G. Wolfer, J. Computer-Aided Mater. Des. 14 **(**2007) 403-417.

[8] F. Ham, Journal of Applied Physics 30 **(**1959)

[9] D. Seif and N.M. Ghoniem, J. Nucl. Mater. 442 **(**2013) S633-S638.

[10] Z. Chang, P. Olsson, D. Terentyev and N. Sandberg, J. Nucl. Mater. 441 **(**2013) 357-363.

[11] Z. Chang, D. Terentyev, N. Sandberg, K. Samuelsson and P. Olsson, J. Nucl. Mater. 461 **(**2015) 221-229.

[12] K. Morishita, Nuclear Instruments and Methods in Physics Research, Section B: Beam Interactions with Materials and Atoms 255 **(**2007) 41-46.

[13] H. Rouchette, L. Thuinet, A. Legris, A. Ambard and C. Domain, Comput. Mater. Sci. 88 **(**2014) 50-60.

[14] B.C. Skinner and C.H. Woo, Phys. Rev. B 30 **(**1984) 3084-3097.

[15] C. Domain and C. Becquart, Phys. Rev. B 65 **(**2002) 024103.

[16] http://fp7-matisse.eu/

[17] C.H. Woo, B.N. Singh and A.A. Semenov, J. Nucl. Mater. 239 **(**1996) 7-23.

[18] A.D. Brailsford and R. Bullough, J. Nucl. Mater. 44 **(**1972) 121-135.

[19] D. Terentyev and L. Malerba, J. Nucl. Mater. 377 **(**2008) 141-146.

[20] Y.N. Osetsky and D.J. Bacon, Model. Simul. Mater. Sci. Eng. 11 **(**2003) 427-446.

[21] C.S. Becquart, K.M. Decker, C. Domain, J. Ruste, Y. Souffez, J.C. Turbatte and J.C. Van Duysen, Radiation Effects and Defects in Solids 142 **(**1997) 9-21.

[22] S.L. Dudarev and P.M. Derlet, J. Phys. Condens. Matter 17 **(**2005) 7097.

[23] D. Terentyev, D.J. Bacon and Y.N. Osetsky, Philos. Mag. 90 **(**2010) 1019-1033.

[24] D. Terentyev and A. Bakaev, J. Nucl. Mater. 442 **(**2013) 208-217.

[25] A. Bakaev, D. Terentyev, G. Bonny, T.P.C. Klaver, P. Olsson and D. Van Neck, J. Nucl. Mater. 444 **(**2014) 237-246.

[26] R. Bullough, M. Wood and E. Little, ASTM Special Technical Publication **(**1981) 593-609.

[27] Y. Katoh, A. Kohyama and D. Gelles, J. Nucl. Mater. 225 **(**1995) 154-162.

# 3. Molecular dynamics studies of possible influence of slip band interaction with nanostructural defects on irradiation creep in F/M alloys

This section describes the work performed at KIT.

## 1. Introduction

The formation of dynamic slip bands in iron was observed mostly during molecular dynamics simulations of microcrack propagation in iron (e.g. [1-5]). In some loading conditions it turned out to be a much easier stress relaxation mechanism enabling local plastic deformation at the crack tips and counteracting brittle fracture [4,5]. More detailed investigations have demonstrated that nucleation and expansion of slip bands is a general phenomenon that can originate from different stress concentrators (and even without them) and be even less energy consuming mechanism of plastic deformation than the common mechanisms based on dislocation mobility. An example of a slip band nucleated and expanded from crack tips is shown in Fig. 1.

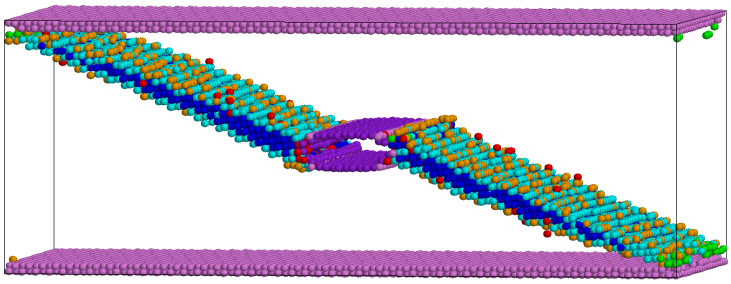

Fig. 1. An example of dynamic slip bands (dark blue regions confined within blue atimic planes) in the MD simulation cell with a microcrack (crack surface colored violet). From Ref. [5].

In contrast to the well-known macroscopic slip bands that are produced, as commonly believed, by long – range dislocation glide along a band of parallel slip planes, the dynamic slip bands are independent entities that have little in common with dislocations. They are typically nucleated on stress concentrators (e.g. scratches on surfaces, microcrack nuclei at grain boundaries, etc.) and can expand only along some lattice planes, including (11-2) and (110), which means that the selection of the plastic deformation mode (i.e. via dislocation motion or dynamic slip band expansion) is very sensitive to the particular loading conditions. Typically, when the external strains promote shear along such lattice planes, the emission and propagation of slip bands requires ~60-70% lower shear stress than the emission of full edge dislocations. The dynamic slip band propagation can thus potentially contribute to creep, where the loads on material are high, but still below the yield strength limit. As far as the local stress conditions on the above-mentioned special slip planes become sufficient to launch slip bands, quick plastic deformation can occur even though the dislocation glide remains strongly suppressed.

Unfortunately, the very special geometry of MD simulations cells used to simulate crack propagation is too restrictive in order to understand the behavior of the dynamic slip bands and their contribution to plastic deformation of iron at larger length scales. Moreover, very little is known about the interaction of propagating dynamic slip bands with various microstructural defects that are known to play important part in creep, acting as barriers that pin dislocations and require thermal or irradiation induced unpinning to enable dislocation motion and hence strain accumulation. Hence the main task of the current modeling was the investigation of dynamic slip bands in simulation cells with different shapes and different relations between the applied stress and the lattice crystal axes.

During the study, the molecular dynamics was applied to iron nanosized plates using the semi-empirical potential of Ackland et al. [6] and the MD code LAMMPS [7]. The simulated slabs had initially orthorhombic geometry with the axes along the simulation cell axes. Periodic boundary conditions were assumed in one of the directions normal to the loading one, making the simulation cell pseudo-infinite in this direction. In the other normal direction the thickness of the simulated slab remained finite and several nanometers less than

the simulation box size in this direction. The straining was achieved by the deformation of the simulation cell as a whole, using the cell deformation algorithm implemented in LAMMPS. The constant engineering strain rate mod was used during all simulations. In the case of uniaxial deformation the atoms in two thin regions ('clamps') at the opposite simulation cell ends along the strain direction were 'frozen' (i.e. they moved only at the moments of cell extension, so that the deformation within clamps was always uniform and corresponded to the acquired nominal strain); the 'frozen' atoms interacted with the other atoms in the lattice in a regular way, but did not shift from their positions. Two straining modes were considered, shear and uniaxial extension. Several slab geometries with different iron lattice orientations in the slab were studied. In order to create a preferential place for slip band or dislocation emission, a V-shaped notch of several atomic monolayers deep was cut at one of free surfaces of each studied slab prior to the stretching. The total numbers of atom in the simulated slabs depended on the particular lattice orientations, but generally were at the level of $(4\div6)\times10^5$ atoms. For each simulation cell geometry, simulations were done at 10 K, in order to exclude the effect of temperature. Simulations at finite temperatures (RT and 600 K) were also undertaken, but the general picture remains nearly the same, differing only in details that are not reported here.

## 2. Results

Given below is a short presentation of the obtained results.

### 2.1 Shear of simulation cell [100]-[010]-[001]

Let us start with the plate-like configuration, where the <100> iron lattice axes were aligned along of the simulation cell edges. The configuration is referred to below as [100]-[010]-[001], where the lattice axes orientations are aligned so as to correspond to the x, y, and z axes of the Cartesian coordinate system of the simulation cell. The simulation cell prior to the onset of the uniaxial straining along the x-axis is illustrated in Fig. 2.

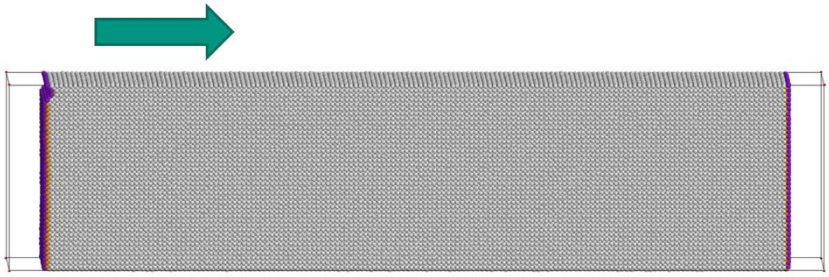

Fig. 2. Simulation cell for configurations [100]-[010]-[001]. Lattice atoms are shown with white spheres; surface and subsurface atoms are purple and orange, respectively. Simulation cell edges are depicted with gray lines. The shear direction is shown with an arrow.

As the shear strain reaches ~0.45 %, one observes the emission of a dynamic slip band, starting at the notch and propagation in the [10-1] direction approximately on (101) plane (see Fig.3 (a). The slip band expands very quickly and already after ~40 ps transverses the plate, as shown in Fig. 3(b). Note that due to the slip band propagation direction being inclined with respect to x-axis and the periodic boundary conditions, the slip band leaves several traces within the simulation cell. As appropriate to this kind of a slip band, the crystal lattice inside the band transforms into fcc one. With the loading progress the relative width of the slip bands increases at the expense of the original material.

Two interesting observations are worth mentioning. First of all, strain stabilizes fcc lattice structure inside the slip bands, in spite of the fact that fcc lattice is unstable at low temperature in general and for the used potential in unstrained cells in particular. Second, the slip band propagation and expansion does not produce any other structural defects, such as point defects and dislocations.

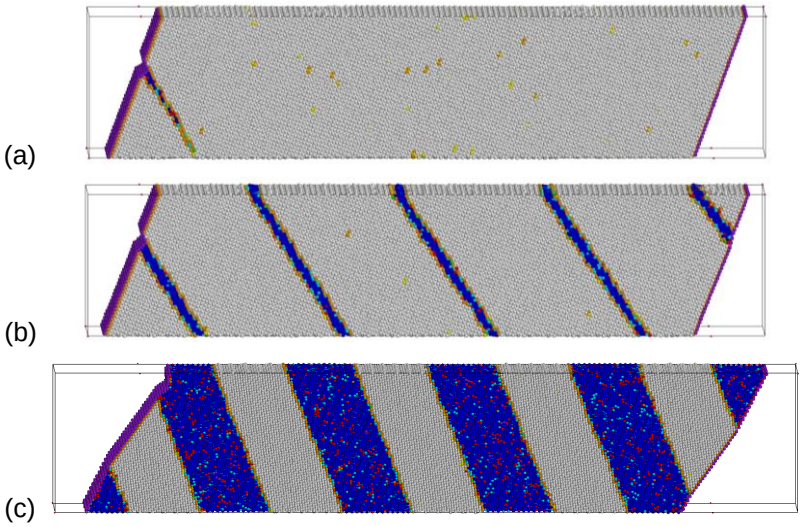


Fig. 3. Consecutive stages of slip band evolution in [100]-[010]-[001] simulation cell. (a) Slip ban nucleation. (b) After penetration through the simulation cell. (c) Slip band thickness increase (here at the shear strain of ~16 %). Atom coloring reflects the topology of the local atomic environment; in particular atoms with the bcc short-range ordering are colored white, while those with the fcc environment are blue.

## 2.2 Shear of simulation cell [111] - [11-2] - [1-10]

This simulation cell is differently oriented with respect to the shear strain. None the less, the general picture of slip bans expansion looks quite similar to the previous case, though the slip system is different (slip on (112) plane in <111> direction in local inclined coordinates) and the slip band itself is a multilayer twin, see Fig. 4. As can be seen, the band is nucleated at the step in the free surface (Fig.4(a)) and propagates through the plate until the opposite plate surface is reached (Fig.4(b)). As a result, the lattice in the cell remains mostly bcc, but divided into domains with twinned lattice orientations. With the strain increase, the twin boundaries move so that the new phase domain grows at the expense of the initial phase. Due to the periodic boundary conditions, this leads eventually to the meeting of the opposite twin boundaries and their annihilation. Eventually, the simulation cell restores a single grain bcc lattice with an orientation rotated with respect to the original one.

Even though the single crystallinity is finally restored, the slip ban expansion is accompanied with the production of a certain number of point defects, mostly point defects (vacancies and interstitials), as can be noticed in Fig. 4(d).

In order to investigate the interaction of propagating slip bands with microstructural defects, similar simulations were undertaken in a simulation cell containing a spherical cavity, as shown in Fig. 5(a). The cavity was positioned so that the propagating slip band would cut it approximately in the middle.

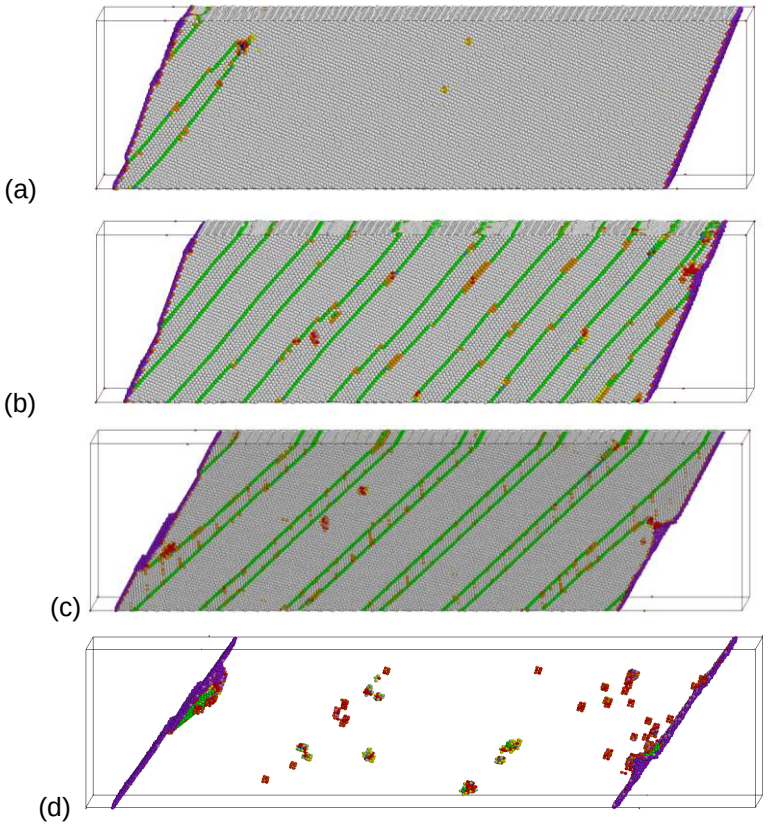


Fig. 4. Consecutive stages of slip band evolution in [111] - [11-2] - [1-10] simulation cell. (a) Slip band nucleation. (b) After penetration through the simulation cell. (c) Slip band thickness increase. (d) Damage remaining after the elimination of the slip band. Regular bcc lattice atoms are hidden and one observes only differently colored atoms with imperfect local atomic environments that surround vacancies and interstitial atoms.

After the application of the shear strain, the initial stages of slip band emission were similar to those in a cavity-free cell. That is multilayer slip band confined within two parallel twin boundaries was propagating through the cell, Fig. 5(b). Note that Fig. 5 does not show the atoms with local bcc environment and so the interior atoms in slip bands, which are also bcc, are not shown as well; only atoms at the slip band boundaries are visible. Interaction of the slip band with the cavity does not stop the slip band, which continues to propagate until the free surface layer is reached, Fig. 5(c). However, there appears a ‘shadow’ behind the cavity, where no slip band exists, Fig. 5(d). In other words, cavities cut an expanding slip band into finite-width strips that propagate independently. An additional effect observed during the slip band cutting of the cavity was the emission of pieces of gliding dislocations from the cavity surface.

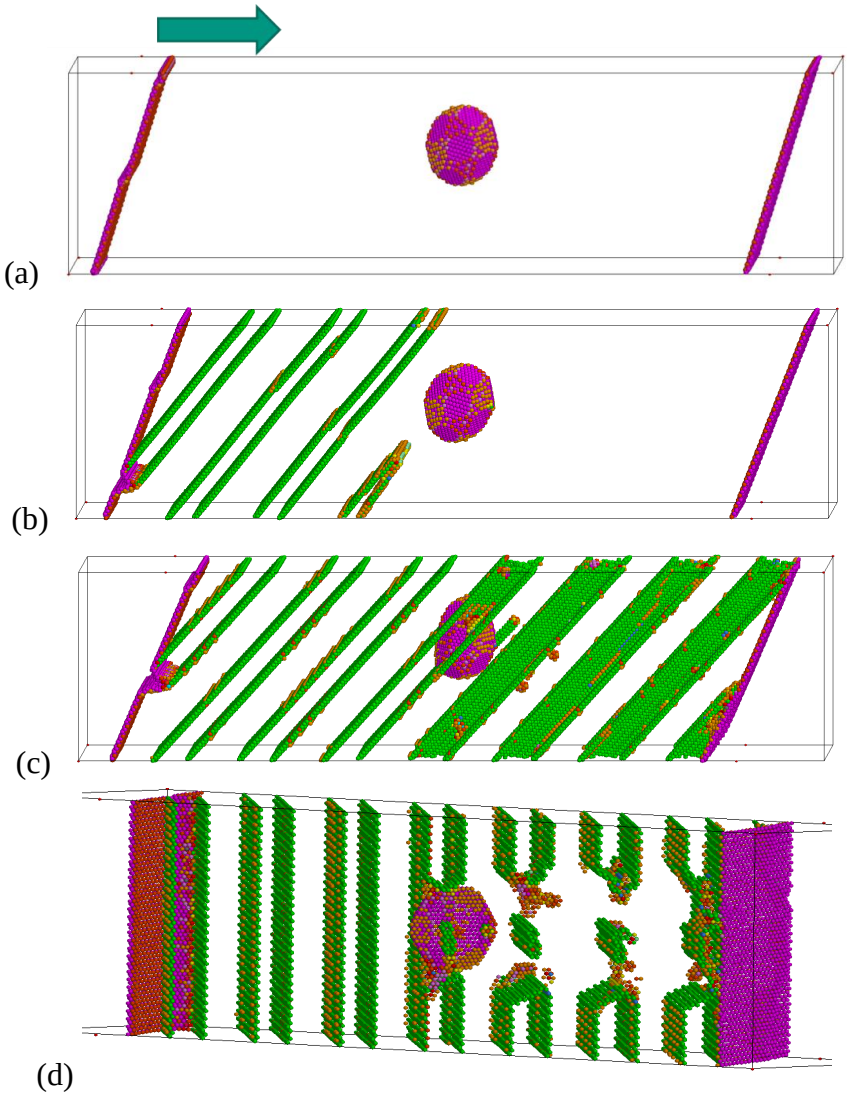


Fig. 5. Interaction of shear bans with a spherical cavity (cavity surface colored violet). Atoms with regular bcc environment are hidden so that only the defects were visible. (a) An early stage of straining. Arrow shows shear direction. (b) Slip band propagation prior to encounter with the cavity. (c) Shear band after the penetration through the plate. (c) Same as (c), but viewed from the bottom along the slip band propagation plane.

## 2.3 Shear of simulation cell [100]-[011]-[01-1]

The expected slip system in this simulation cell was the same as in case (ii), that is slip on (112) plane in <111> direction. However, the strain causes shear in the opposite direction. It is well known that this slip system is asymmetric with respect to the shear direction and can either promote or prevent slip band formation. The shear in the current case is in the ‘anti-slip’ direction, so that the emission of a slip band requires higher strain than the emission of full edge dislocations. The preferable emission of edge dislocation and their glide were indeed observed during simulations, but the discussion of the observation is out of the scope of this report. Here it is worth mentioning only one simulation whose results contribute to the elucidation some features of slip band behavior as well.

As shown in Fig. 6(a), at a certain strain two dislocation half-loops are formed at the notch, gliding on two equivalent (11-2) planes. Dislocations are visible at the left layer surface; the upper dislocation glides downwards and the lower one - upwards. One can notice that two dislocations are somewhat different. The upper dislocation keeps a compact core, so that the dislocation segment in Figs 6(b to d) looks nearly as a point in profile. In contrast, the lower dislocation moves in a ‘dissociated’ mode with a visible trail behind it (shown in green in panels (b) and (c)). As a result, a number of vacancies are left in the dislocation wake on the glide plane (visible in Fig. 6 as small clusters of atoms around vacancies that have non-bcc

environment). Due to periodic boundary conditions, the upper dislocation crosses many times the upper/lower face of simulation cell and the gliding plane of the lower dislocation. Fig. 6(b) shows the moment, when the non-dissociated dislocation is going to cross the gliding plane just in front of the trailing partial of the dissociated dislocation. As a result, the trailing partial loses the ability to move, but the leading partial continues advancing. As we know from the modeling of plastic zone formation before the crack tip [5], this is just the proper condition for slip band formation. And indeed the stacking fault behind the leading partial gradually transforms into a slip band, while it moves towards the right free surface: Fig. 6(c). Moreover, when the right end of the slip band is fixed on the surface, nothing prevents the trailing partial movement in the reverse direction, which is favorable for slip band propagation, Fig. 6(d). So one observes the 'reverse' formation of a multi-twin slip band connecting the opposite layer surfaces, while the trailing partial transforms into a full dislocation that remains within the band of the new phase (this dislocation segment is seen in the upper part of Fig. 6(e) between two (green) twin boundaries confining the reoriented bcc phase.

Overall, Fig. 6(e) looks much like Fig. 4(c) and one would expect the subsequent thickness increase of the slip band as the straining proceeds. The picture turns out to be more complicated. As one can notice in Fig. 6(c), the upper dislocation, while moving downwards, has to cross the dissociated part ('trail') behind the other dislocation. This does not happen, however. Instead, the upper dislocation slows down and only after some straining becomes forced up to the twin boundary. There it stops (since there is no appropriate slip direction in the twinned lattice in the slip band) and, moreover, completely prevents the sideways movement of the twin boundary as a whole, blocking the propagation of the kinks along the twin boundary surface. Correspondingly, the thickening of the slip band with the strain increase is due to only the free twin boundary. This communicates an important message: the sideways expansion of slip band can be seriously affects by properly oriented dislocations captured on the slip band interfaces.

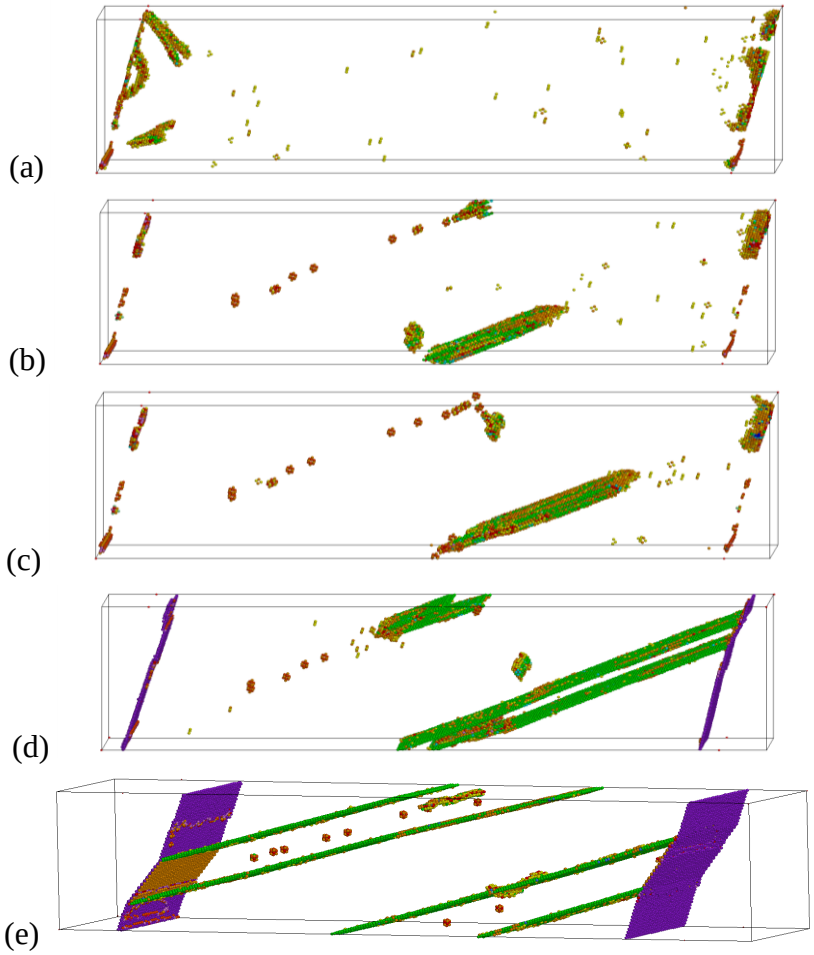


Fig. 6. Shear deformation of simulation cell [100]-[011]-[01-1]. Similar to Fig.5, atoms with regular bcc environment are hidden. (a) Emission of two gliding half-loop dislocations on equivalent slip planes (at the left surface), (b) Immediately before crossing the trail of the right dislocation (moving upwards) by the left dislocation (moving downwards). (c) At 3 ps after the crossing. (d) Slip band starts expanding in the reverse direction. (d) After the full separation into domains with twinned orientations. One can notice multiple point

defects and two segments of dislocation lines. The cell is in a slightly different orientation as compared to the other panels in the figure.

## 2.4 Tensile deformation of [100] - [011] - [01-1] layer

Finally, let us consider a somewhat different situation, where an iron layer is subject to uniaxial tension along the [100] crystal layer, as shown in Fig. 7a. The layer has a notch in the middle, which serves as initiation place for slip bands. In one half of the cell, a cavity is added in order to study the interaction of expanding slip bands with this obstacle type.

As expected, at sufficient stress level two slip bands are emitted from the notch, Fig. 7(b). The slip bands in this case are of multi-twin type.

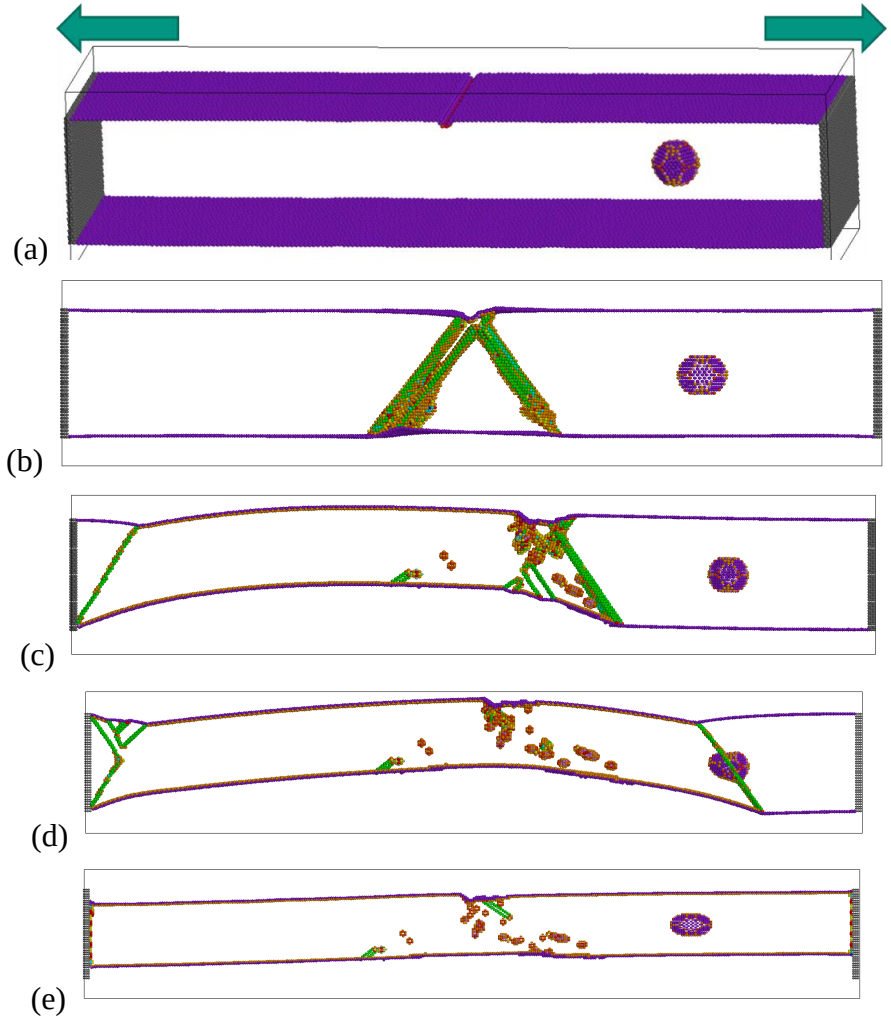


Fig. 7. Different stages of one-dimensional tension of a layer with lattice orientation [100] - [011] - [01-1]. Atoms with the regular bcc short-range environment are hidden. (a) Initial simulation cell. Tension direction is shown with arrows. (b) After emission of two slip bands from the notch. (c) At the moment when the left-side twin boundary reaches the 'clamp'. (d) The right slip band boundary crosses the cavity. (e) final configuration with single-crystal layer.

With further straining, one observes the thickening of one of these two bands (in the figure – the left one) as a result of sideways glide of the outer twin boundary until it reaches the clamp. Then the possibilities for strain relaxation by this moving twin boundary are exhausted and the other slip band starts to expand, Fig. 7(c).

The 'secondary' boundary movement occurs on the right slab side, where the cavity is located, but the cavity has little effect on the 'pinning' of the right twin boundary; the latter is due rather to the damage inside the

slip band itself, which requires some extra stress to 'release' the twin boundary, This extra stress cannot accumulate as long as the left twin boundary moves and relaxes the slab.

Similar to the left twin boundary, the right twin boundary drifts after unpinning in the right direction until the right clamp is reached. The cavity gives little resistance to the boundary drift and no 'hole' in the boundary remains after the cavity is passed. The only visible result is the elongation of the cavity in the tension direction that is due to the lattice reorientation behind the twin boundary. After long enough loading, all twin boundaries disappear and the layer restores single-crystallinity, Fig. 7(e), reaching ~40% strain. This indicates that slip band expansion, if not hindered by internal barriers (such as dislocation) can promote extremely high superplastic deformation.

## 3. Summary

Summing up, the current study shows that slip bands are emitted from local stress concentrators and demonstrate two modes of expansion: first, there occurs quick propagation of a narrow slip band through the thickness of the simulation cell, followed by remarkably slower expansion in thickness as a result of slip band boundary shift. Both types of slip band expansion are matter conservative and as such cannot be directly accelerated by irradiation. On the other hand, the irradiation creates in the material large numbers of structural defects (point defects, dislocations, cavities), which to that or other degree affect the slip band expansion. While **point defects:** seem to have no effect on either slip band nucleation, or expansion, the dislocations are able to strongly pin slip band boundaries. Cavities are shown to partially block the propagation of thin slip bands, but have little effect on the sidewalk shift of slip band boundaries.

In relation to irradiation creep, the effect of radiation can be similar to that encountered in the 'climb + glide' mechanism of dislocation-based creep, where radiation both creates and removes additional barriers that pin the propagation of local strain carriers.

## 4. References for section 3

[1] A. Machova, G.J. Ackland, Model. Simul. Mater. Sci. Eng. 6 (1998) 521.

[2] Y.-F. Guo, C.-Y. Wang, D.-L. Zhao, Mater. Sci. Eng. A349 (2003) 29.

[3] A. Spielmannova, A. Machova, P. Hora, Comput. Mater. Sci. 48 (2010) 296.

[4] V.A. Borodin, P.V. Vladimirov, J. Nucl. Mater. 416 (2011) 49.

[5] V.A. Borodin, P.V. Vladimirov, J. Nucl. Mater. 442, suppl.1 (2013) 49.

[6] G.J. Ackland, M.I. Mendelev, D.J. Srolovitz, *et al*, J. Phys.: Condens. Matter 16 (2004) S2629.

[7] S. Plimpton, J. Comp. Phys. 117 (1995) 1–19.